Kinase-controlled phase transition of membraneless organelles in mitosis

Rai, Arpan Kumar ; Chen, Jia-Xuan ; Selbach, Matthias ; Pelkmans, Lucas

Abstract: Liquid–liquid phase separation has been shown to underlie the formation and disassembly of membraneless organelles in cells, but the cellular mechanisms that control this phenomenon are poorly understood. A prominent example of regulated and reversible segregation of liquid phases may occur during mitosis, when membraneless organelles disappear upon nuclear-envelope breakdown and reappear as mitosis is completed. Here we show that the dual-specificity kinase DYRK3 acts as a central dissolvase of several types of membraneless organelle during mitosis. DYRK3 kinase activity is essential to prevent the unmixing of the mitotic cytoplasm into aberrant liquid-like hybrid organelles and the over-nucleation of spindle bodies. Our work supports a mechanism in which the dilution of phase-separating proteins during nuclear-envelope breakdown and the DYRK3-dependent degree of their solubility combine to allow cells to dissolve and condense several membraneless organelles during mitosis.

DOI: https://doi.org/10.1038/s41586-018-0279-8

Kinase-controlled phase transition of membrane-less organelles in mitosis

Arpan Kumar Rai[1], Jia-Xuan Chen[2,3], Matthias Selbach[2,4], Lucas Pelkmans[1*]

[1]Department of Molecular Life Sciences, University of Zurich
[2]Max Delbrück Center for Molecular Medicine, Berlin
[3]Present address: Cancer Research UK Cambridge Institute, University of Cambridge
[4] Charité-Universitätsmedizin Berlin, Berlin
*Correspondence to: Lucas Pelkmans (lucas.pelkmans@imls.uzh.ch)

Summary

Liquid-liquid phase separation has been recognized to underlie the formation and disassembly of liquid, membrane-less organelles in cells, but cellular mechanisms that control this phenomenon remain poorly understood. A prominent example of regulated and reversible segregation of liquid phases may occur during mitosis, when membrane-less organelles disappear upon nuclear envelope breakdown and reappear as mitosis is completed. Here we show that the dual-specificity kinase DYRK3 acts as a central dissolvase of several types of membrane-less organelles during mitosis. DYRK3 kinase activity is essential to prevent the unmixing of the mitotic cytoplasm into aberrant liquid hybrid organelles and the over-nucleation of spindle bodies. Our work supports a mechanism in which the dilution of phase-separating proteins during nuclear envelope breakdown and the DYRK3-dependent degree of their solubility allow cells to dissolve and condense several membrane-less organelles during mitosis.

A fundamental property of inhomogeneous crowded fluids is their ability to display coacervation, electrostatically-driven liquid-liquid phase separation of molecules that can lead to the emergence of micro-compartments[1,2]. This phase separation paradigm has in recent years been successfully applied to explain the formation of numerous membrane-less organelles in cells, driven by intrinsically disordered regions in proteins and weak multivalent interactions[3–5], and often aided by polymeric scaffolds such as RNA to which these proteins bind[6,7], and which themselves can induce phase separation[8]. However, as with all cellular processes, various gene functions and enzyme activities must have evolved to modulate the underlying physicochemical phenomenon, to drive it out of equilibrium, or push it across critical boundaries to make it advantageous for living systems.

We previously discovered that upon cellular stress, the dual-specificity kinase DYRK3 partitions into stress granules via its intrinsically disordered N-terminal domain and that its kinase activity is required for the dissolution of stress granules, likely by phosphorylating multiple RNA-binding proteins[9]. Subsequently, it was shown that MBK-2, the *C. elegans* homologue of DYRK3, controls the dissolution of P-granules during the first cell division of the embryo[10]. In addition, POM1, a *S. pombe* relative of DYRK3, displays reversible clustering[11] and controls the presence of protein assemblies involved in cytokinesis[12], which may also involve phase separation. Thus, DYRK-family kinases could represent a novel class of evolutionarily conserved cellular regulators that control phase transition phenomena in cells, serving various cell-physiological purposes.

A particularly dramatic example of such control may occur during mitosis. It is long known that numerous membrane-less organelles in both the cytoplasm and the nucleus disappear during mitosis, or, in the case of stress granules, cannot be induced to form in mitotic cells[13–15]. However, the physical principles and the molecular mechanisms behind these phenomena have remained unclear. We here investigate whether DYRK3 acts as the dissolvase in these processes, and how this is coordinated with the cell cycle.

DYRK3 interactome and localization

To identify proteins interacting with DYRK3 in unperturbed cells, we performed quantitative affinity purification using stable isotope labelling with amino acids in cell culture (SILAC)-based quantitative proteomics[16]. From two independent label swap experiments (forward and reverse) (Extended Data Fig. 1a), we identified a total of 251 proteins interacting specifically with transiently overexpressed GFP-tagged DYRK3 (Fig. 1a, Table S1). The majority (86%) of these proteins are known to bind RNA, and amongst them are also multiple components of stress granules, splicing speckles, and the centrosome or pericentriolar matrix (Fig. 1a). Moreover, when we treated cells with GSK-626616, a small compound inhibitor of DYRK3[9], many of these interactions became more prominent (Fig. 1b, Extended Data Fig. 1b,c and Table S2), which were not caused by an increase in the abundance of interactors or DYRK3 itself (Extended Data Fig. 1d,e).

Overexpression of DYRK3 leads to its spontaneous phase separation at a specific concentration threshold[9]. To investigate its subcellular localization at near-endogenous levels, we created an inducible cell line. At very low induction levels (~30% of endogenous levels) (Extended Data Fig. 2a), GFP-DYRK3 shows a diffuse distribution within the nucleus and the cytoplasm, but also an enrichment in centrosomes (Pericentrin) and pericentriolar matrix (PCM1) (Fig. 1c), and in splicing speckles (SC35) (Fig. 1d). Inhibition of DYRK3 leads to a further accumulation in splicing speckles, and to a visible increase in splicing speckle size (Fig. 1d). Consistent with our previous findings[9], GSK-626616-inhibited GFP-DYRK3 also accumulates in arsenite-induced stress granules (PABP1) at these low expression levels (Extended Data Fig. 2b). In mitotic cells, we observed that GFP-DYRK3 localizes to spindle poles, and that it accumulates in small granules that grow in size when its kinase activity was inhibited (Fig. 1e and Extended Data Fig. 2c).

Mitotic effects of DYRK3 inhibition

Since DYRK3 associates with membrane-less organelles in both the nucleus and the cytoplasm, accumulates in granules in mitotic cells when inhibited, and interacts with proteins that are heavily phosphorylated during mitosis, of which some sites are sensitive to DYRK3 inhibition[9] (Extended Data Fig. 2d), we decided to investigate its role during mitosis, when the contents of both cellular compartments mix. Strikingly, we found that inhibition of DYRK3 in mitotic cells leads to aberrant condensations of splicing speckle marker SC35 (Fig. 2a and Extended Data Fig. 3a), stress granule marker PABP (Fig. 2b and Extended Data Fig. 3b) and pericentriolar matrix protein PCM1 (Fig. 2c and Extended Data Fig. 3c). Aberrant condensations were observed in two different human cell lines and for multiple markers (Extended Data Fig. 3d-f). Importantly, testing a panel of inhibitors of kinases known to regulate centrosome biogenesis or splicing speckle composition in interphase cells did not show these effects (Extended Data Fig. 3g). Moreover, GSK-626616 does not cause the

accumulation of SRPK1[17] or CDK1, a key regulator of entry into mitosis, in these aberrant condensations, nor does it affect their activation or activity inside cells (Extended Data Fig. 4a-f) or *in vitro*[9], while RNAi-mediated knockdown of DYRK3 recapitulated the GSK-626616 effects (Extended Data Fig. 4g).

Interestingly, splicing speckle, stress granule, and pericentriolar matrix markers co-condensed into the same hybrid structures, which also stained positive for poly-adenylated RNA and accumulated inhibited DYRK3 (Fig. 2d,e and Extended Data Fig. 5a,b). Not all markers of membrane-less organelles condensed into these structures, since P-bodies, nucleoli, and Cajal bodies appeared to dissolve normally during mitosis when DYRK3 is inhibited (Extended Data Fig. 5c-e). The aberrant condensates are not classical aggresome-like structures, since they do not stain positive for ubiquitin (Extended Data Fig. 5f). Timelapse analysis of mitotic granule formation using mCherry-tagged SRRM2, a splicing speckle protein, revealed that they appear fast (within 15-20 min) upon DYRK3 inhibition (Fig. 2f and Supplementary Video 1) and display liquid-like merging (Extended Data Fig. 6a), while photobleaching the granules showed that SRRM2 exchanges rapidly ($t_{1/2}$ ~10 sec) and completely between the condensed and dissolved phases (Fig. 2g). The total amount of SRRM2 in cells did not change during granule formation (Extended Data Fig. 6b), and the accumulation of SRRM2 in the condensed phase was a consequence of its depletion from the dissolved phase (Extended Data Fig. 6c). Thus, DYRK3 kinase activity is essential during mitosis to prevent the formation of aberrant liquid-liquid phase-separated hybrid condensates consisting of nuclear and cytoplasmic proteins and RNA, by keeping the condensation threshold of its substrates high.

DYRK3 dissolvase activity

To prevent aberrant condensation, DYRK3 may act as a dissolvase of multiple liquid-unmixed compartments. When we overexpressed wildtype GFP-DYRK3 in interphase cells, we observed dissolution of splicing speckles in the nucleus (Fig. 3a,b and Extended Data Fig. 7a). This dissolving effect was dependent on its kinase activity, as it was reversed by treating cells with the DYRK3 inhibitor, and was not observed when overexpressing a kinase-dead point mutant of GFP-DYRK3 (Fig. 3a,b and Extended Data Fig. 7a,b). Moreover, a nuclear localization sequence mutant of DYRK3 prevented the dissolution of splicing speckles, while exclusive nuclear localization of DYRK3 completely dissolved splicing speckles, indicating the requirement for direct interaction with its substrates (Extended Data Fig 7c,d).

Similarly, we found that overexpression of GFP-DYRK3 dissolves pericentriolar satellites and prevents the induction of stress granules with arsenite in the cytoplasm in a kinase activity-dependent manner (Fig 3c-f and Extended Data 7e-h). Furthermore, phase-separated structures formed by overexpressing an intrinsically disordered domain of PCM1 (1-1468)[14] and SRRM1, a highly intrinsically disordered interactor of DYRK3 and known splicing speckle component (Extended Data Fig. 7i), are completely dissolved by DYRK3 in a kinase-dependent manner (Extended Data Fig. 7j-l). We did not observe a dissolving effect of overexpressed DYRK3 on nucleoli (Extended Data Fig. 7m), consistent with the observation that these organelles still dissolve in DYRK3-inhibited mitotic cells. This shows that kinase-active DYRK3 has dissolvase activities for multiple but not all membrane-less organelles, both in the cytoplasm and in the nucleus.

DYRK3 to substrate ratio drives phase transition

Upon entry into mitosis, membrane-less organelles disappear, and then re-appear during telophase or after completion of mitosis[13–15,18]. If disappearance occurs through a dissolution process driven by DYRK3, then its dissolvase activity must rapidly increase at the beginning of mitosis and then reduce at the end of mitosis. When we analysed the protein levels of endogenous DYRK3 along the cell cycle, we observed that its expression increases as cells progress from late S to the end of G2 (Fig. 4a). Yet, cells in late G2 display splicing speckles in the nucleus and can condense stress granules in the cytoplasm upon stress[13,15,18]. Furthermore, we did not observe a sudden increase in DYRK3 levels as cells enter mitosis (black box in Fig. 4a).

One explanation could be that the concentration of DYRK3 relative to its substrate suddenly increases upon nuclear envelope breakdown. This occurs because key substrates of DYRK3 are exclusively located in either the nucleus (SRRM1) or the cytoplasm (PCM1), resulting in their dilution when the compartment barrier is removed (Fig. 4b and Extended Data Fig. 8a-d). And because DYRK3 itself is located in both compartments and does not get similarly diluted, the DYRK3 to substrate ratio increases by a factor of 2-3 (Fig. 4b) as cells transition from G2 into M. To investigate whether such an increase in ratio is necessary and sufficient to ensure complete dissolution of membrane-less organelles during mitosis, we transiently transfected inducible wildtype GFP-DYRK3 along with mCherry-SRRM1 in non-mitotic cells. From a large number of single cells covering a wide range of expression levels and DYRK3 to SRRM1 ratios, we determined an intracellular phase diagram of SRRM1 in a condensed or dissolved phase as a function of DYRK3 and SRRM1 levels. This revealed a remarkably sharp phase boundary at a specific DYRK3 to SRRM1 ratio across a large range of expression levels, below which SRRM1 would be condensed and above which it would be dissolved (Fig. 4c). Furthermore, by following interphase cells through time-lapse imaging, we could observe how changes in concentration of the components determines granule phase behaviour as mapped in the phase diagram. Cells in which the DYRK3 to SRRM1 ratio increased over time displayed a sudden transitioning from a condensed SRRM1 phase to a dissolved phase when the phase boundary was crossed (Cell 1 and 2 in Fig 4d). While SRRM1 remained dissolved in cells that always displayed a high DYRK3 to SRRM1 ratio and stayed above the phase boundary over time (Cell 3 in Fig. 4d).

We next focussed on single cells with low, near-endogenous levels of GFP-DYRK3 and mCherry-SRRM1 that entered mitosis during the time-lapse recording. When we plotted single-cell time-traces of DYRK3 to SRRM1 ratios into the phase diagram, and marked when SRRM1 becomes dissolved, we observed that this occurs right at the moment of crossing the phase transition boundary (Cell 1 and 2 in Fig. 4e), due to the sudden, 2.7-fold increase in DYRK3 to SRRM1 ratio during the G2-to-M transition (marked by arrowheads in Fig. 4e). Consistently, when we followed a cell with high levels of overexpressed SRRM1 and a consequently very low DYRK3 to SRRM1 ratio far away from the phase transition boundary, the 2.7-fold increase in ratio during the G2-to-M transition was not sufficient to cross the boundary, resulting in the persistence of SRRM1 granules in mitotic cells (Cell 3 in Fig. 4e). We observed this effect invariably in single cells that overexpress SRRM1 beyond a critical concentration, at which point levels of endogenous DYRK3 were insufficient to trigger a phase transition upon mitotic entry (Fig. 5a). These cells show mitotic SRRM1 granules (Fig. 5a) that recruit endogenous splicing speckle proteins

(Extended Data Fig. 8e), which also undergo liquid-like merging, and show rapid exchange of SRMM1 between the condensed and dissolved phase, which is under the control of DYRK3 (Extended Data Fig. 8f, g). Furthermore, we observed that the dilution effect alone is not sufficient. When we arrested cells in mitosis after nuclear envelope breakdown with a single thymidine-nocodazole block, and splicing speckles are dissolved, acute treatment with the DYRK3 inhibitor results in the appearance of aberrantly condensed structures (Extended Data Fig. 8h), indicating that DYRK3 kinase activity is required to maintain the dissolved phase during mitosis.

Aberrant granules delay mitotic progression

We next asked whether the aberrant co-condensation of proteins in mitotic cells has a consequence for mitotic progression. We found that when cells are treated with the DYRK3 inhibitor, they display a prolonged mitotic length, and often a mitotic arrest (Fig. 5a). Interestingly, we also found a prolonged mitotic length in cells that were unable to completely dissolve mitotic granules upon nuclear envelope breakdown due to very high levels of overexpressed SRRM1, even when DYRK3 activity was not compromised (Fig. 5a). This suggests that mitotic defects are, in part, caused by an inability to keep proteins dissolved in mitotic cells. Strikingly, while centrosome duplication appears to occur normally in DYRK3-inhibited cells, gamma-tubulin displays multiple condensation foci (Extended Data Fig. 9a), resulting in the frequent occurrence of multipolar spindles (Fig. 5b). To explain this, we searched the DYRK3 interactome for possible mitotic regulators that might have an impact on mitosis. This revealed that BuGZ (ZNF207) and its interaction partner Bub3, are enriched in the DYRK3 interactome upon GSK-626616 treatment (Fig. 5c). BuGZ is required for spindle matrix assembly through liquid-liquid phase separation[19], and localizes to splicing speckles in interphase cells[20] (Extended Data Fig. 9b). When we analysed its localization in mitotic cells, we found that upon DYRK3 inhibition, also BuGZ becomes sequestered in mitotic granules where it co-localizes with inhibited DYRK3 (Extended Data Fig. 9c, d) and PABP (Fig. 5c). Thus, DYRK3 releases mitotic regulators from liquid-unmixed compartments at the onset of mitosis and keeps them dissolved during mitosis. When this is compromised, such mitotic regulators are sequestered in mitotic granules, which interferes with their normal roles during mitosis leading to mitotic defects.

At the end of mitosis, reassembly of the nuclear envelope and the re-accumulation of DYRK3 substrates in their respective compartments should lead to a drop in the DYRK3 dissolvase to substrate ratio below the critical point and reverse this process. However, some membrane-less organelles, such as splicing speckles, re-condense already in telophase[18], before the nuclear envelope has been reassembled. Strikingly, we noticed that DYRK3 is abruptly degraded at the boundary between M and G1 (red box in Fig. 4a and Fig. 5d), suggesting that re-condensation before nuclear envelope reassembly may rely on rapidly removing DYRK3. Progression through mitosis and entry into G1 is driven by the Anaphase Promoting Complex/Cyclosome (APC/C complex), which promotes the ordered ubiquitination and subsequent degradation of multiple D-box (RXXL)-containing substrates through mitosis[21]. We found that DYRK3, which contains a D-box, interacts with both APC/C co-activators Cdc20 and Cdh1, resulting in its targeting to ubiquitin-positive aggregates in the cytoplasm and its degradation (Fig. 5e and Extended Data Fig. 10a-d), consistent with the identification of DYRK3 as a novel APC/C substrate[22]. Moreover, when we overexpressed GFP-DYRK3 in mitotic cells to levels that cannot be degraded by

APC/C, splicing speckles remain dissolved in telophase, indicating that APC/C-mediated degradation of DYRK3 at the end of mitosis is involved in their re-condensation process (Extended Data Fig. 10e).

Discussion

We have here uncovered a mechanism by which multiple membrane-less organelles dissolve during mitosis and re-condense as mitosis completes. The dual-specificity kinase DYRK3 plays a key role in this process by acting as the dissolvase of these organelles. This extends our previous finding that DYRK3 dissolves stress granules during stress recovery[9]. Importantly, not all membrane-less organelles that disappear during mitosis, such as P-bodies and nucleoli, are dissolved by DYRK3. This may suggest a different physico-chemical phenomenon that underlies the formation of these organelles, or a role for other kinases, possibly relatives of DYRK3, that mediate their dissolution.

The organelles that are dissolved by DYRK3 all contain protein and RNA, and form by liquid-liquid phase separation. DYRK3 binds to proteins that are key components of these organelles, and is a proline-directed kinase with broad specificity[23] that phosphorylates multiple serine and threonine residues in unstructured domains[9]. This may affect the electrostatic properties of these domains such that it alters the condensation threshold of these proteins. When the active concentration of DYRK3 becomes high enough relative to its substrates, it triggers a transition from the condensed to the dissolved phase, which will remain to exist as long as this ratio stays sufficiently high. The ratio can be modulated in multiple ways. At the onset of mitosis, the loss of the nucleus-cytoplasm compartment boundary is exploited to alter the DYRK3 to substrate ratios such that it results in a phase transition. For some organelles, degradation of the dissolvase is used to trigger a phase transition in the opposite direction. Thus, progression through the cell cycle can be conceived as a process where cells cycle through a phase diagram (Fig. 6). Also, when compartment boundaries stay intact, a specific accumulation or depletion of substrate in one compartment may alter the ratio sufficiently to induce a phase transition which may occur during cellular stress[24]. In addition, the ratio could be altered by increasing the abundance or activity of DYRK3 by specific upstream regulators, which could be coupled to different physiological processes such as the cell cycle[23,25] .

We currently do not understand how at the end of mitosis, and upon degradation of DYRK3, aberrant co-condensation is prevented. One possibility is that the kinetics or regulation of dephosphorylation of DYRK3-phosphorylated residues in proteins is component- or compartment-specific, as may be the levels of dephosphorylation required to initiate phase transition. In addition, since cytoplasm and nucleus compartment boundaries become re-established right at this time, which may contribute to preventing aberrant co-condensation.

Multiple aspects of mitosis are compromised when the DYRK3 to substrate ratio cannot display its natural dynamics. Its increase allows the release of mitotic regulators from liquid-unmixed compartments as cells enter mitosis and prevents their aberrant co-condensation during mitosis. In addition, preventing co-condensation during mitosis could be important to ensure homogeneous distribution of proteins and RNA between daughter cells during symmetric cell division, which may then be additionally regulated to achieve differential condensation points in daughter cells

during asymmetric cell division[10,26]. Finally, through its ability to control the condensation of multiple compartments, DYRK3 may link structural and functional roles for RNA, transcription, and splicing to the assembly of the mitotic spindle[27–29], and be involved in the maintenance of the pericentriolar matrix. We propose that DYRK family kinases represent an evolutionarily conserved novel class of regulators that control liquid-liquid unmixing phenomena in cells crucial for a variety of cell-physiological processes.

References

1. Overbeek, J. T. G. & Voorn, M. J. Phase separation in polyelectrolyte solutions. Theory of complex coacervation. . *J. Cell. Comp. Physiol* **49,** 7–26 (1957).
2. Banani, S. F., Lee, H. O., Hyman, A. A. & Rosen, M. K. Biomolecular condensates: organizers of cellular biochemistry. *Nat. Rev. Mol. Cell Biol.* **18,** 285–298 (2017).
3. Brangwynne, C. P. *et al.* Germline P Granules Are Liquid Droplets That Localize by Controlled Dissolution/Condensation. *Science (80-.).* **324,** 1729–1732 (2009).
4. Kato, M. *et al.* Cell-free formation of RNA granules: Low complexity sequence domains form dynamic fibers within hydrogels. *Cell* **149,** 753–767 (2012).
5. Li, P. *et al.* Phase transitions in the assembly of multivalent signalling proteins. *Nature* 336–340 (2012). doi:10.1038/nature10879
6. Zhang, H. *et al.* RNA Controls PolyQ Protein Phase Transitions. *Mol. Cell* **60,** 220–230 (2015).
7. Saha, S. *et al.* Polar Positioning of Phase-Separated Liquid Compartments in Cells Regulated by an mRNA Competition Mechanism. *Cell* **166,** 1572–1584.e16 (2016).
8. Jain, A. & Vale, R. D. RNA phase transitions in repeat expansion disorders. *Nature* **546,** 243–247 (2017).
9. Wippich, F. *et al.* Dual specificity kinase DYRK3 couples stress granule condensation/ dissolution to mTORC1 signaling. *Cell* **152,** 791–805 (2013).
10. Wang, J. T. *et al.* Regulation of RNA granule dynamics by phosphorylation of serine-rich, intrinsically disordered proteins in C. elegans. *Elife* **3,** (2014).
11. Saunders, T. E. *et al.* Noise Reduction in the Intracellular Pom1p Gradient by a Dynamic Clustering Mechanism. *Dev. Cell* **22,** 558–572 (2012).
12. Rincon, S. A. *et al.* Pom1 regulates the assembly of Cdr2-Mid1 cortical nodes for robust spatial control of cytokinesis. *J. Cell Biol.* **206,** 61–77 (2014).
13. Spector, D. L. & Smith, H. C. Redistribution of U-snRNPs during mitosis. *Exp. Cell Res.* **163,** 87–94 (1986).
14. Dammermann, A. & Merdes, A. Assembly of centrosomal proteins and microtubule organization depends on PCM-1. *J. Cell Biol.* **159,** 255–266 (2002).
15. Sivan, G., Kedersha, N. & Elroy-Stein, O. Ribosomal slowdown mediates translational arrest during cellular division. TL - 27. *Mol. Cell. Biol.* **27 VN-r,** 6639–6646 (2007).
16. Ong, S.-E. *et al.* Stable Isotope Labeling by Amino Acids in Cell Culture,

SILAC, as a Simple and Accurate Approach to Expression Proteomics. *Mol. Cell. Proteomics* **1,** 376–386 (2002).
17. Gui, J. F., Lane, W. S. & Fu, X. D. A serine kinase regulates intracellular localization of splicing factors in the cell cycle. *Nature* **369,** 678–682 (1994).
18. Thiry, M. Behavior of interchromatin granules during the cell cycle. *Eur. J. Cell Biol.* **68,** 14–24 (1995).
19. Jiang, H. *et al.* Phase Transition of Spindle-Associated Protein Regulate Spindle Apparatus Assembly. *Cell* **163,** 108–122 (2015).
20. Wan, Y. *et al.* Splicing function of mitotic regulators links R-loop-mediated DNA damage to tumor cell killing. *J. Cell Biol.* **209,** 235–246 (2015).
21. Sivakumar, S. & Gorbsky, G. J. Spatiotemporal regulation of the anaphase-promoting complex in mitosis. *Nat. Rev. Mol. Cell Biol.* **16,** 82–94 (2015).
22. Merbl, Y. & Kirschner, M. W. Large-scale detection of ubiquitination substrates using cell extracts and protein microarrays. *Proc Natl Acad Sci U S A* **106,** 2543–2548 (2009).
23. Aranda, S., Laguna, A. & de la Luna, S. DYRK family of protein kinases: evolutionary relationships, biochemical properties, and functional roles. *FASEB J.* **25,** 449–62 (2011).
24. Kedersha, N. L., Gupta, M., Li, W., Miller, I. & Anderson, P. RNA-binding proteins TIA-1 and TIAR link the phosphorylation of eIF-2?? to the assembly of mammalian stress granules. *J. Cell Biol.* **147,** 1431–1441 (1999).
25. Cheng, K. C. C., Klancer, R., Singson, A. & Seydoux, G. Regulation of MBK-2/DYRK by CDK-1 and the Pseudophosphatases EGG-4 and EGG-5 during the Oocyte-to-Embryo Transition. *Cell* **139,** 560–572 (2009).
26. Pellettieri, J., Reinke, V., Kim, S. K. & Seydoux, G. Coordinate activation of maternal protein degradation during the egg-to-embryo transition in C. elegans. *Developmental Cell* **5,** 451–462 (2003).
27. Blower, M. D., Feric, E., Weis, K. & Heald, R. Genome-wide analysis demonstrates conserved localization of messenger RNAs to mitotic microtubules. *J. Cell Biol.* **179,** 1365–1373 (2007).
28. Chan, F. L. *et al.* Active transcription and essential role of RNA polymerase II at the centromere during mitosis. *Proc. Natl. Acad. Sci.* **109,** 1979–1984 (2012).
29. Grenfell, A. W., Heald, R. & Strzelecka, M. Mitotic noncoding RNA processing promotes kinetochore and spindle assembly in Xenopus. *J. Cell Biol.* **214,** 133–141 (2016).

Supplementary Information

Supplementary Figure 1.

Source data for gels

Table. S1

List of detected DYRK3 specific interaction partners.

Table. S2

List of detected DYRK3 specific interaction partners upon GSK-626616 inhibitor treatment

Supplementary Video 1

SRRM2-mCherry granule formation upon GSK-626616 inhibitor treatment

HeLa cell expressing SRRM2-mCherry was arrested in mitosis by thymidine-nocodazole block. Time-lapse movie shows SRRM2 granule formation on addition of GSK-626616 (1 μM). Time point (0 min) corresponds to GSK-626616 addition. Scale bar is 10 μm. Movie is representative of atleast three independent experiments.

Acknowledgments
We thank Pelkmans and Klemm lab members for discussions. We further thank Jean Michael peters, Andreas Merdes and Magdalini Polymenidou for reagents and acknowledge the assistance and support of the Center for Microscopy and Image Analysis, University of Zurich for performing FRAP experiments. EMBO and HFSP LTF supported A.K.R. J.X.C was supported by MDC-NYU PhD exchange program fellowship. L.P. is supported by the Swiss National Science Foundation and the University of Zurich.

Author contributions
L.P. conceived the project. L.P. and A.K.R. wrote the paper. A.K.R performed and analysed the data. J.X.C. performed SILAC pull-down experiments and bioinformatic data analysis and was supervised by M.S..

Competing financial interests
The authors declare no competing financial interests.

Materials & Correspondence
Lucas Pelkmans

Main Figure Legends

Figure 1. DYRK3 interacts with multiple membrane-less compartments

a
Scatter plot of DYRK3-specific interactors determined by double-SILAC pull-down and MS.
b
Examples of DYRK3 interactions that increase upon GSK-626616 treatment. Error bar represents the standard error of the median. (n) indicates the number of peptide evidence ratios included for calculating the protein ratio in one triple-SILAC pull-down.
c
Colocalization of GFP-wildtype (WT) DYRK3 with centrosomes.
d
Colocalization of GFP-wildtype (WT) DYRK3 with splicing speckles and increase upon GSK-626616 treatment (1μM, 2hrs).
e
Mitotic cells show formation of DYRK3-positive granules (arrowheads) upon GSK-626616 treatment (1μM, 4hrs).

Images are representative of at least three independent experiments. Scale bars: 10 μm

Figure 2. Formation of mitotic hybrid compartments upon DYRK3 inhibition

a
Top: Mitotic SC35 granules upon GSK-626616 treatment (1μM, 1hr).
Bottom: Quantification of metaphase SC35 granule number (3 independent experiments).
b
Top: Mitotic PABP granules upon GSK-626616 treatment (1μM, 3hr).
Bottom: Quantification of metaphase PABP granule number (3 independent experiments).
c
Top: Mitotic PCM1 granules upon GSK-626616 treatment (1μM, 6hr).
Bottom: Quantification of metaphase PCM1 granule number (3 independent experiments).
d
Colocalization of splicing and stress granule markers in hybrid compartments in mitotic cells upon GSK-626616 treatment (1μM, 6hr).
e
Colocalization of splicing and pericentriolar satellite markers in hybrid compartments in mitotic cells upon GSK-626616 treatment (1μM, 6hr).
f
Time-lapse images show SRRM2-mCherry granule formation upon GSK-626616 (1μM) treatment in cells arrested in mitosis.
g
FRAP trajectories of mitotic SRRM2-mCherry granules in presence of GSK-626616 (1μM). Images show FRAP recovery. Data are Mean ± SD.

Box plots: central mark: population median; box: interquartile range; whiskers: 1st/3rd quartile ± 1.5* interquartile range; outliers: dots. Statistical analysis performed across cells by Welch two-sided t-test.

Data and images are representative of at least three independent experiments. Scale bars: 10 μm.

Figure 3. DYRK3 over-expression dissolves membrane-less compartments

a
Splicing speckle dissolution upon overexpressing wildtype (WT) DYRK3, and not kinase-dead (K218M) DYRK3.
b
Quantification of splicing speckle dissolution.
c
Pericentriolar satellite dissolution upon overexpressing wildtype (WT) DYRK3, and not kinase-dead (K218M) DYRK3.
d
Quantification of pericentriolar satellite dissolution.
e
Stress granule dissolution upon overexpressing wildtype (WT) DYRK3, and not kinase-dead (K218M) DYRK3. Arsenite treatment (500μM, 45mins).
f
Quantification of stress granule dissolution.

* denotes transfected cells. Data and images are representative of at least three independent experiments. Data are Mean ± SD. Scale bars: 10 μm.

Figure 4. Increase in DYRK3 to substrate ratio during mitosis drives dissolution of phase-separated compartments

a
Western blot analysis of endogenous DYRK3 levels in cells synchronized in mitosis (thymidine-nocodazole) and released for indicated times.
b
Left: Nuclear intensity change during G2 to M transition. GFP-wildtype DYRK3 (green), mCherry-SRRM1 (red) and GFP-wildtype DYRK3: mCherry-SRRM1 ratio (blue). Data are Mean ± SD (n= 9 cells, 3 independent experiments). 0 min refers to nuclear envelope breakdown.
Right: Time-lapse images of a cell (single Z-stack) transitioning from G2 to M.
c
GFP-wildtype DYRK3 and mCherry-SRRM1 nuclear intensities for a population of cells.
Data points (single cells): colour-coded for SRRM1 state.
d
Left: Trajectory of three interphase cells expressing inducible GFP-wildtype DYRK3 and mCherry-SRRM1, mapped onto the phase diagram of Fig. 4C. The trajectories are colour coded for fraction of SRRM1 granules compared to first time point (TP:01).
Right: Time-lapse images of the cells shown in the left panel.
e
Left: Trajectory of three cells expressing inducible GFP-wildtype DYRK3 and mCherry-SRRM1 transitioning through cell-cycle stages, mapped on the phase diagram (Fig. 4C). The trajectories are colour coded for cell cycle stages and fraction of SRRM1 granules compared to first time point (TP:01). Inset: DYRK3: SRRM1 ratio plotted for the three trajectories. Arrowheads show G2 to M transition.
Right: Time-lapse images of the cells shown in the left panel.

Data in Fig. 4 a, c-e are representative of two independent experiments. Scale bars: 10 μm.

Figure 5. Mitotic defects on DYRK3 inhibition and APC/C dependent degradation of DYRK3

a

Top left: Mitotic length plotted as a function of mCherry-SRRM1 nuclear intensity (in G2 phase). Data points (single cells): colour-coded for metaphase SRRM1 state.

Top right: Increase in mitotic length upon GSK-626616 treatment (1μM) (3 independent experiments).

Bottom: Time-lapse images of cells marked in the top panel.

b

Formation of aberrant granules and multipolar spindles in mitotic cells upon GSK-626616 treatment (1μM, 6hrs).

c

Left: Increase in the interaction of DYRK3 with BUB3 and ZNF207 upon GSK-626616 treatment. Error bar represents the standard error of the median. (n) indicates the number of peptide evidence ratios included for calculating the protein ratio in one triple-SILAC pull-down experiment.

Right: Co-localization of spindle matrix and stress granule markers in mitotic cells upon GSK-626616 treatment (1μM, 3hr).

d

Western blot quantifications of the relative density of DYRK3 during M and early G1 (M+2 hrs). Data are Mean ± SD.

e

Top: DYRK3 interacts with APC/C co-activators Cdc20 and Cdh1. HA-Cdh1 and HA-Cdc20 probed with anti-HA antibody. GFP and GFP-DYRK3 probed with anti-GFP antibody.

Bottom: Endogenous DYRK3 is degraded by overexpressed HA-Cdh1 and HA-Cdc20 (3μg, 48hr) in HEK293T cells.

Box plots: central mark: population median; box: interquartile range; whiskers: 1st/3rd quartile ± 1.5* interquartile range; outliers: dots. Statistical analysis performed across cells by Welch two-sided t-test.

Images and data are representative of at least three independent experiments. Scale bars: 10 μm

Figure 6.

Model showing membrane-less organelles transitioning through a phase diagram during the cell cycle**.** DYRK3 perturbation shifts the phase boundary resulting in the formation of hybrid compartments in mitotic cells.

Methods

Cell culture

HeLa cells were a kind gift from Marino Zerial (MPI-CBG, Dresden), Hela-FlpIn-Trex cells were a kind gift from Ivan Dikic (Goethe University, Frankfurt)[30] and HEK293T cells were from ATCC (Molsheim Cedex). Hela and HEK293T cells were maintained in 10-cm dishes in DMEM supplemented with 10% fetal bovine serum (Sigma-Aldrich) and L-Glutamine (Sigma-Aldrich). Hela-FlpIn-Trex cells were maintained in 10-cm dishes in DMEM supplemented with 10% tetracycline-free fetal bovine serum (Clonetech Laboratories), L-Glutamine and blasticidin (1μg/mL, Santa Cruz). Hela-FlpIn-Trex expressing GFP-wildtype DYRK3 was induced using doxycycline (Sigma) with indicated time and concentration. All cells were maintained in a humidified incubator at 37^0C under 5% CO_2. All cell lines were regularly tested for Mycoplasma contaminations. Test results were negative. For imaging experiments, cells were grown in 96-well plates (Greiner Bio-One International).

Inhibitors

GSK-626616 (PubChem CID: 15981157) was obtained from Tocris Bioscience. DMSO was from Sigma-Aldrich (D2438). The following inhibitors were used in this study: GW 843682X (Tocris Bioscience, 2977), ZM 447439 (Tocris Bioscience, 2458), Barasertib (Selleck chemicals, S1147), Volasertib (Selleck chemicals, S2235), VX-680 (Selleck chemicals, S1048), TCA 2317 HCl (Tocris Bioscience, 4066), KHCB19 (Tocris Bioscience, 4262), KHCB19 (Calbiochem, Merck Millipore, 219511), TG003 (Tocris Bioscience, 4336), SRPIN340 (Santa Cruz, sc-394310) and SRPIN340 (Tocris Bioscience, 5063). Prior to inhibitor treatments, cells were washed and serum deprived for 2 hrs.

Generation of Hela-FlpIn-Trex expressing GFP-wildtype DYRK3

Hela-FlpIn-Trex cells were co-transfected with plasmids, pcDNA5/FRT/TO-GFP-wildtype DYRK3 and Flp recombinase expression vector (pOG44) for 48 hrs, and then selected with hygromycin (250μg/mL, Thermo Fisher Scientific) for two weeks. Monoclonal cells were isolated by limiting-dilution technique, and then expanded.

SILAC cell culture

HEK293T cells (ATCC, Manassas, USA) were cultivated using SILAC DMEM media (Life Technologies) containing ("light") Lys-0: L-lysine-$^{12}C_6{}^{14}N_2$, Arg-0: L-arginine-$^{12}C_6{}^{14}N_4$, or ("medium") Lys-4: L-lysine-$^{12}C_6{}^{14}N_2{}^2D_4$, Arg-6: L-arginine-$^{13}C_6{}^{14}N_4$, or ("heavy") Lys-8: L-lysine-$^{13}C_6{}^{15}N_2$, Arg-10: L-arginine-$^{13}C_6{}^{15}N_4$ and supplemented with 10% dialyzed fetal bovine serum (PAA Laboratories, Cölbe, Germany), 4 mM Glutamax and 1 mM sodium pyruvate. Cells were maintained in a humidified incubator under 5% CO_2 at 37°C.

SILAC quantitative pull-down assays

To study interaction partners of DYRK3, a label-swap SILAC pull-down experiment was set up as depicted in Extended data Fig. 1a. Plasmids containing EGFP only or EGFP- wildtype DYRK3 were transiently transfected into SILAC-labelled HEK293T cells using linear polyethylenimine (PEI) transfection reagent (Polysciences, Warrington, PA). Cells of different SILAC states were harvested 48 h post-transfection and lysed separately using a Dounce homogenizer in lysis buffer containing 25 mM Tris/HCl pH 7.4, 125 mM KCl, 1 mM $MgCl_2$, 1 mM EGTA/KOH pH 8.0, 5% glycerol, 1% Triton X-100 and freshly added protease inhibitor cocktail (Roche). The cleared lysates were then incubated with anti-GFP agarose beads (Chromotek) at 4 °C for 90 min. After that, the beads were washed two times in buffer I (25 mM Tris/HCl pH 7.4, 125 mM KCl, 1 mM $MgCl_2$, 1 mM EGTA/KOH pH 8.0, 5% glycerol, 0.1% Triton X-100) followed by one wash in buffer II (1 mM Tris/HCl pH 7.4, 150 mM KCl, 1 mM $MgCl_2$). Beads of different SILAC states were combined during the final washing step. Proteins were then eluted by heating the beads to 90 °C in 8 M guanidinium chloride and precipitated in ethanol at 4 °C.
A separate triple-SILAC pull-down experiment was carried out to study the impact of DYRK3 inhibitor (GSK-626616) on DYRK3 interactions as shown Extended data Fig. 1b. Briefly, 24 h post-transfection, cells were further treated with or without 10 µM GSK-626616 inhibitor for 2 h. The remaining steps of the pull-down experiment were then conducted as described above.
Precipitated proteins were resolubilized in 6M urea/2M thiourea buffer (10 mM HEPES pH 8.0). Proteins were then reduced by dithiothreitol and akylated by iodoacetamide in the dark, followed by sequential digestion in solution using lysyl endopeptidase (Lys-C, Wako) for 3 h and trypsin (Promega) overnight at room temperature as reported previously[31]. Peptides were desalted and purified by solid phase extraction in C18 StageTips[32].

Liquid chromatography tandem mass spectrometry
Peptide separation was done online by reversed phase chromatography using an in-house packed column (inner diameter: 75 µm; ReproSil-Pur C18-AQ 3-µm resin, Dr. Maisch GmbH) through a 120-min gradient of acetonitrile (8-50%) with 0.1% formic acid at a nanoflow rate of 200 nl/min. Eluted peptides were sprayed directly by electrospray ionization into a Q Exactive Plus Orbitrap mass spectrometer (Thermo Scientific). Mass spectra were acquired in data-dependent mode using a top10 sensitive method. Each duty cycle consisted of one full scan (resolution: 70,000, target value: 3×10^6, scan range: 300 to 1,700 m/z) and 10 MS/MS scans of fragment ions produced via higher energy collision dissociation (HCD; resolution: 35,000, target value: 5×10^5, maximum injection time: 120 ms, isolation window: 4.0 m/z). Precursor ions with unassigned or +1 charge state were not selected for fragmentation scans. Dynamic exclusion time was 30 s.

Mass spectrometry data processing
All mass spectrometry raw data were processed using MaxQuant software package (version 1.5.5.1)[33] with built-in Andromeda search engine[34]. Spectral data were searched against a target-decoy database containing the forward and reverse protein sequences of UniProt human proteome release 2016_06 (92,578 entries), EGFP and the default list of 245 common contaminants. Corresponding SILAC labels were selected for the double- or triple-SILAC experiment. A maximum of 3 SILAC labelled amino acids were allowed for each peptide. Trypsin/P specificity was assigned. Carbamidomethylation of cysteine was chosen as fixed modification.

Methionine oxidation and protein N-terminal acetylation were set as variable modifications. A maximum of 2 missed cleavages were tolerated. Minimum peptide length of 7 amino acids was required. Each protein group must contain at least one unique peptide. False discovery rate (FDR) was set to 1% for both peptide and protein identifications.
For SILAC protein quantification, minimum ratio count was set to one. Both the unique and razor peptides were used for quantification. The "re-quantify" function was switched on. The "advanced ratio estimation" option was also chosen.

Bioinformatic data analysis
All data analyses were performed in R statistical environment (version 3.3.1). To normalize the pull-down data, protein ratios were first log-transformed. Under the assumption that the majority of detected proteins were non-specific background binders, the distribution of protein ratios was assessed using kernel density estimation to find the peak density. Protein ratios were then normalized by adjusting to the point at which peak density was found. Further for the triple-SILAC pull-down data, proteins were filtered to retain only those with a normalized H/L or M/L $\log_2$ ratio greater than the cut-off value of 1. The log-transformed H/M ratios were then re-scaled with respect to the DYRK3 H/M ratio (Extended data Fig. 1c).
Gene ontology annotation for categorizing the detected DYRK3 interaction partners was downloaded on 28th June 2016 from the QuickGO database[35] provided by the European Bioinformatics Institute. The list of stress granule components was obtained from a review article[36].
To assess phosphorylation level changes of detected DYRK3 specific binders during cell cycle, quantitative phosphoproteomic data of human cell cycle were downloaded from Olsen et al. (2010)[37]. The data were filtered sequentially to retain: 1) phospho-sites with high confidence in localization probability (class I)[38]; 2) phospho-sites that were regulated over cell cycle (changed by at least two folds from highest to lowest amounts); 3) phospho-sites belonging to proteins that were identified as DYRK3 specific interaction partners in current study. The phospho-site ratios already normalized by changes in protein abundance were then re-scaled by z-score transformation and plotted as a heat map (Extended data Fig. 2d).
The standard error of the median in Fig. 1 and Fig. 5 was computed based on the bootstrap (1,000 times) sampling distribution of corresponding log-transformed ratios of peptide evidence. Protein ratio of ZNF207 in Fig. 5c is determined by a regression analysis using the "advanced ratio estimation" function in MaxQuant.
Prediction of protein low complexity region (LCR) was performed using the SEG algorithm with default parameters[39].

Cell synchronization
Cells were synchronized in mitosis (M) by treatment with 2mM thymidine (Sigma-Aldrich) for 22 hrs, then washed thrice with PBS and released from thymidine block for 5 hrs in fresh medium, followed by nocodazole (25ng/mL) (Sigma-Aldrich) treatment for 14 hrs. For time-course experiments, mitotic cells were harvested by shake-off, followed by a 3 min centrifugation at 300xg. Cells were then washed thrice with normal medium and released in normal medium for indicated times.

Plasmids
Generation of full-length DYRK3 plasmids, pcDNA5-GFP-wildtype DYRK3 and pcDNA5-GFP-K218M DYRK3 has been reported earlier[9] . pcDNA5-SV40NLS-

wildtype DYRK3 and pcDNA5-SV40NLS-K218M DYRK3 constructs were generated by annealing oligonucleotides 5'-CCGGTTACCGAAGAAGAAGCGAAAGGTACA-3' and 5'-TTACCGAAGAAGAAGCGAAAGGTACACCGG-3', followed by ligation into pcDNA5-GFP-wildtype DYRK3 and pcDNA5-GFP-K218M DYRK3 plasmids using AgeI restriction site. pcDNA5-GFP-wildtype DYRK3-NLS mutant plasmid was generated by site-directed mutagenesis using primer pair 5'-GCTTGTGGGGGGTCGCTCAGCTGCGGGTGCAGCGGCGGGTCCCCCAGGCAGC-3' and 5'-GCTGCCTGGGGGACCCGCCGCTGCACCCGCAGCTGAGCGACCCCCCACAAGC-3'. mCherry-SRRM1 was generated by amplifying SRRM1 from Flag-SRRM1[40] (Addgene plasmid, #11305) using primer pair 5'-GCTAAGCTTCGATGGACGCGGGATTTTTCCGCGGAAC-3' and 5'-CATGGTACCTTATTAAGACTGTGGGGACACTTGGGCCTTC-3', followed by insertion into mCherry2-C1 plasmid (kind gift from Michael Davidson, Addgene plasmid # 54563) using HindIII and KpnI restriction sites. pcDNA5/FRT/TO-GFP-wildtype DYRK3 vector was generated by amplifying GFP-DYRK3 from pcDNA5-GFP-wildtype DYRK3 using primer pair 5'-GGTGGTACCCGCCACCATGGTGAGCAAGGGCG-3' and 5'-GCTGGATCCTTATTA GCTAATCAGTTTTGGCAATACACT-3', followed by insertion in pcDNA5/FRT/TO plasmid[9] using KpnI and BamHI restriction sites. RFP-wildtype DYRK3 and RFP-K218M DYRK3 were generated by amplifying them from pcDNA5-GFP-wildtype DYRK3 and pcDNA5-GFP-K218M DYRK3 respectively, using primer pair 5'-ATCGAATTCTATGAAGTGGAAAGAGAAGTTGGGGGATG-3' and 5'-GGTACCTTATTAGCTAATCAGTTTTGGCAATACAC-3', followed by insertion into mRFP-C1 plasmid (kind gift from Robert Campbell, Michael Davidson & Roger Tsien, Addgene plasmid # 54764) using EcoRI and KpnI restriction sites. Full–length SRRM2 (NM_016333.3) was synthesized by Genscript (NJ, USA) and inserted into mCherry2-N1 plasmid (kind gift from Michael Davidson, Addgene plasmid # 54517) using KpnI and AgeI restriction sites. GFP-PCM1 (1-1468) was a kind gift from Andreas Merdes. EGFP-3XNLS[41] was a gift from Dyche Mullins (Addgene plasmid, # 58468). pmScarlet_NES_C1[42] was a gift from Dorus Gadella (Addgene plasmid, # 85060). 1436 pcDNA3-Flag-HA was a gift from William Sellers (Addgene plasmid # 10792). HA-Cdh1[43] and HA-Cdc20[43] were a gift from Marc Kirschner (Addgene plasmid # 11596).

Plasmid Transfections

Transfections were performed with indicated plasmids with genejuice reagent (EMD Millipore) or Lipofectamine 2000 (Thermo-Fischer Scientific) as per manufacturer instructions**.**

RNA FISH

Fluorescent in situ hybridization (FISH) was performed with ATTO 488-labelled 18-nucleotide long oligo-dT probe (Microsynth) for detecting polyA-mRNA. Probe hybridization was performed using reagents and protocol provided by the manufacturer (LGC Biosearch Technologies). Cells were grown in 96 well plates, fixed by adding 4% PFA for 10 mins, followed by permeabilization with 70% ethanol for 6 hrs at 4^0C. Cells were then washed with wash buffer, and incubated with the

probe in hybridization buffer for 6 hrs at 37°C. The cells were washed again with wash buffer and then processed for immunofluorescence as described below.

RNAi

Cells were reverse-transfected using Lipofectamine RNAimax (Thermo-Fischer Scientific) according to manufacturer instructions, and grown in 96 well plates. Three silencer-select siRNA for DYRK3 (5'-CGGAUUUUGGAGCAUCUUA-3', 5'-CCAUCUAGCUUAUCGAUAU-3'and 5'-GAAAAGACAUGGAGUUAUU-3') were pooled together (Thermo-Fischer Scientific). Positive (KIF11) and negative control silencer-select siRNA were from Thermo-Fischer Scientific. 1pmol siRNA was added per well of a 96 well plate. Cells were fixed 72hrs post transfection.

Imaging

Imaging was carried out on an automated spinning disk microscope from Yokogawa (Cell Voyager 7000), with an enhanced CSU-X1 spinning disk (Microlens-enhanced dual Nipkow disk confocal scanner, wide view type), a 40× 0.95 NA Olympus objective, a 60x 1.2 NA Olympus water-immersion objective and Andor sCMOS cameras (Andor, 2,560 × 2,160 pixels). Live cell imaging experiments were performed with Yokogawa (Cell Voyager 7000) with 60x1.2 NA Olympus water-immersion objective. All cells were maintained in a humidified environment at 37^0C under 5% CO_2 for live imaging experiments. For nucleo-cytoplasmic dilution experiments (Fig. 4b and Extended data Fig. 8a-d), Hela-FlpIn-Trex cells were transfected with indicated plasmids for 6 hrs and then synchronized in G1-S by thymidine (2mM, 22hrs) followed by release in normal medium for 6 hrs before imaging. GFP-DYRK3 expression was induced with doxycycline (1μg/mL) for 2 hrs before imaging. Hoechst 33342 (0.5μg/mL, Thermo-Fischer Scientific) was added to stain DNA, an hour before imaging. For nucleo-cytoplasmic dilution experiments, six Z-stacks (1μm apart) were acquired at each time point and data stored as individual stacks. For other experiments, images were stored as maximum intensity projection. For mitotic arrest experiments, plasmids were transfected overnight, followed by thymidine treatment (2mM, 22hrs) and then released in normal medium for 6 hrs. Cells were then treated with nocodozole (25ng/mL) for 6hrs in serum-deprived medium to arrest cells in pro-metaphase. For experiments measuring the mean intensity of SRRM2-mCherry during mitotic granule formation (Extended data Fig. 6 b and c), cells were imaged with 60x1.2 NA objective, and acquired Z stacks (0.45 μm apart, 43 stacks) were stored as individual files. For SRRM2-mCherry and mCherry-SRRM1 granule fusion experiments in mitotic cells, acquired Z-stacks (1 μm apart, 11 stacks) were stored as individual files. For experiments to calculate the mitotic length, Hoechst 33342 (0.5μg/mL, Thermo-Fischer Scientific) was added to stain DNA, an hour before imaging. Time-lapse imaging was performed with time interval of 10 mins.

Image analysis

Images were processed using ImageJ (http://rsb.info.nih.gov/ij/). For quantifying mitotic granules (SC35 granules, PABP granules and PCM1 granules) in metaphase, cells were manually segmented and mean cell intensity was determined for SC35, PABP and PCM1. Granules were determined using FIJI 3D Objects Counter plugin, with an intensity threshold of 2.5 X the mean mitotic cell intensity. We implemented an adjoining pixel cut-off of (8 pixels for SC35 granules, 12 pixels for PABP granules and 16 pixels for PCM1 granules; pixel size 161.3 nm x 161.3 nm)[44]. 90^{th} percentile

of granule numbers for DMSO control data in Fig. 2a and 2b were used as the cut-off for quantification of Extended data Fig. 3g (3 for SC-35 granule and 1 for PABP granule). Mitotic granules were observed and quantified in metaphase (identified based on DAPI staining).

For nuclear dilution experiments of GFP-3xNLS, mCherry-SRRM1 and GFP-DYRK3, the nuclei of cells in G2 phase were segmented based on Hoechst signal. For cytoplasmic dilution experiments of pmScarlet-NES and GFP-DYRK3, nuclear segmentation was performed based on Hoescht signal, and the cell segmentation was performed using the cytoplasmic fluorescent signal from these proteins. For cytoplasmic dilution experiments of PCM1 (1-1468), cells were co-transfected with plasmid expressing mcherry protein. Nuclear segmentation was performed based on Hoescht signal, and the cell segmentation was performed using the cytoplasmic fluorescent signal of mcherry. Mitotic cells were segmented using the fluorescent signal from these proteins. Mean nuclear or cytoplasmic intensity at each time-point is the mean intensity from four Z-stacks (1μm apart). The mean nuclear intensity at each time point was normalized to the intensity at time-point (-60min). For experiments measuring the mean intensity of SRRM2-mCherry during mitotic granule formation (Extended data Fig. 6b and c), sum projection of the Z-stacks (0.45 μm apart, 43 stacks) was performed in Image J. Mitotic cells that were entirely captured within the Z-stacks during the course of the time-lapse movie were used for quantification.
For experiments performed in Extended data Fig. 1d, cell and nuclear segmentation was performed using CellProfiler[45] . Mitotic, border, mis-segmented cells, and cells with multiple nuclei were discarded using supervised machine learning tool, CellClassifier[46]. Mean intensity features were extracted from segmented cells and used for quantification.
Mitotic length was calculated from Prophase/Pro-metaphase to Anaphase based on Hoescht signal. All data analyses were performed in Microsoft Excel and R statistical environment. Exposure and image processing has been performed similarly for all sub-figures in each panel. Images have been rescaled similarly in all sub-figures in a panel except Main Fig. 4e. In Fig. 4e the images of mCherry-SRRM1 in M phase are rescaled differently compared to S and G2 phase for better visualization of condensed and dissolved states of SRRM1. Background subtraction was performed on images by calculating the mean background intensity outside the cells.

Statistical analysis was performed by Welch two-sided t-test in R statistical environment using default t-test function.

Phase diagram experiment
For phase diagram experiment (Fig. 4c, 4d and 4e), Hela-FlpIn-Trex cells were co-transfected with pcDNA5/FRT/TO-GFP-wildtype DYRK3 and mCherry-SRRM1 for 24 hrs and then induced with doxycycline (1μg/mL) for 2 hrs before imaging. Hoechst 33342 (0.5 μg/mL, Thermo-Fischer Scientific) was added to stain DNA, an hour before imaging. Time-lapse imaging was performed with time interval of 15 mins.

Phase diagram (Fig. 4c) was built by randomly selecting cells from multiple time points from the start, middle and end of the time-lapse movie. Nuclear segmentation was manually performed based on Hoescht signal, and the mean nuclear intensity of GFP-DYRK3 and mCherry-SRRM1 was calculated from the maximum intensity

projections. The nuclear intensities were used to determine the phase-diagram. Cells were annotated for SRRM1 granules being in dissolved (≤ 3 granules) or condensed state (> 3 granules). Cells in interphase (Fig. 4d) or cells transitioning from interphase to mitosis (Fig. 4e) from the same time-lapse experiment were mapped on the determined phase diagram.

FRAP Analysis

Hela-FlpIn-Trex cells were grown on 8 well chambers (Ibidi GmbH, Germany). Cells were transfected with indicated plasmids for 24 hours, for experiments in interphase cells. Photo-bleaching experiments in interphase cells were performed in serum-deprived medium. For mitotic experiments, cells were transfected overnight with indicated plasmids, followed by G1-S arrest with thymidine (2mM). mCherry-SRRM1 transfected cells were released in serum-deprived medium and monitored in mitosis. SRRM2-mCherry transfected cells were arrested in mitosis by nocodazole (in serum-deprived medium). Photobleaching was performed on a Leica SP5 Mid UV-VIS equipped with a 63x 1.4 NA, Oil, Plan-Apochromat objective. Cells were maintained at 37^0C under 5% CO_2 during the course of experiment. A defined region was bleached 2 times at full laser power. Recovery could not be monitored for long durations because of mitotic granules moving out in Z-direction. Recovery curves are therefore plotted for durations where the granules seemed not to move in Z-direction. FRAP analysis was performed using ImageJ.

Immunofluorescence

Cells were grown in 96 well plates and fixed by adding 4% PFA (Electron Microscopy Sciences) for 20 mins and then permeabilized with 0.2% Titon-X-100 for 20 mins. The cells were blocked with 1% BSA in PBS (blocking buffer) before incubating with primary antibodies in blocking buffer for 2 hrs at room temperature, followed by incubation with Alexa-Fluor labeled secondary antibody (Life Technologies) in blocking buffer for 1 hour at room temperature. Nuclei were stained using DAPI (Life Technologies). Staining for γ-tubulin and pT446APC3 antibodies, was performed by pre-permeabilizing the cells with 0.1% Triton-X (in PBS) for 3 mins before PFA fixation. Staining of ZNF207 (BugZ) was performed by washing cells with PEM buffer (100 mM PIPES, pH 6.8, 5 mM EGTA, 2 mM MgCl2) and permeabilized with 0.05% Triton-X (in PEM buffer) for 3 mins before PFA fixation[47] (in PEM buffer). Staining for PCM-1 antibody (Cell Signaling, 5259S), was performed by fixing cells with -20^0C methanol for 5 min followed by blocking with 1% BSA. The following antibodies were used: PABP (1:100, Santa Cruz, sc-32318), G3BP (1:500, Abcam, ab56574), Pericentrin (1:400, Abcam, ab4448), SC35 (1:400, Sigma-Aldrich, S4045), PCM1 (1:100, Santa Cruz, sc-67204), PCM1 (1:200, Cell Signaling, 5259S), SRRM2 (1:600, Sigma-Aldrich, HPA041411), γ-tubulin (1:200, Sigma-Aldrich, T6557), SON (1:600, Sigma-Aldrich, HPA023535), SRPK1 (1:200, BD Biosciences, 611072), Cyclin B1 (1:800, Cell Signaling, 12231), CDK1 (1:200, Cell Signaling, 9116), Phospho-CDK1 (Tyr15) (1:50, Cell Signaling, 4539), β-tubulin (1:600, Abcam, ab6046), DDX6 (1:400, Bethyl Laboratories, A300-461A), Coilin (1:400, Abcam, ab87913), Fibrillarin (1:400, Abcam, ab5821), Ubiquitin (FK2) (1:200, Enzo Life Sciences, BML-PW8810), B-23 (1:600, Sigma-Aldrich, B0556), ZNF207 (1:500, Sigma-Aldrich, HPA017013), TIAR (1:200, BD Biosciences, 610352, kindly provided by Magdalini Polymenidou, UZH, Zurich, Switzerland) and phospho-APC3 (T446) (1:200, kindly provided by Jan Michael Peters, IMP, Vienna, Austria).

Western Blotting
Samples were prepared for western blotting, as follows: Cells in culture dishes were washed thrice with PBS before adding lysis buffer (150 mM NaCl, 50 mM HEPES, 1% Triton X-100, 0.1% SDS, 2mM DTT, 5mM EDTA, and 2x protease inhibitor cocktail in miliQ H2O), followed by scraping. Lysates were incubated for 30 mins on ice (with 15 second sonication every 15min). The cells were then centrifuged at 21,000 RCF for 15 min at 4^0C and the supernatant was stored at -80^0C. Proteins in the lysates were denatured by addition of loading buffer and boiling for 10 min. Proteins were resolved by 10% SDS-PAGE and further analyzed by immunoblotting. After wet transfer of proteins onto a PVDF membrane (Immobilon-P, 0.45 μm, Millipore), membranes were incubated in 5% low fat milk in 1XPBST (1XPBS, 0.1% Tween-20) for 1 hour at room temperature. Membranes were then probed with primary antibodies in 3% BSA in 1xPBST for 2 hrs at room temperature, followed by incubation with HRP-conjugated secondary antibodies (1:5000) in 5% low fat milk in 1xPBST for 1 hour at room temperature. For detecting DYRK3, PABP and G3BP membranes were incubated with primary antibody for 24 hrs at 4^0C. Signal was revealed with HRP substrate solution. The following antibodies were used: DYRK3 (1:1000, abcam, ab155949), GFP (1:1000, Cell Signalling, 2956), Pan-Actin (1:1000, Cell Signaling, 8456), CyclinA2 (1:500, Abcam, ab7956), PABP (1:500, Santa Cruz, sc-32318), G3BP (1:1000, Abcam, ab56574), HA (1:1000, Sigma Aldrich, 11867423001) and GFP (1:1000, Cell Signaling, 2956). For quantification, images were processed using ImageJ.

Immunoprecipitation experiments
Cells were collected in lysis buffer lysis buffer (150 mM NaCl, 50 mM HEPES, 1% Triton X-100, 0.1% SDS, 5mM EDTA and 2x protease inhibitor cocktail in miliQ H2O), allowed to lyse on ice for 20 min. The cells were then centrifuged at 21,000 RCF for 15 min at 4^0C and the supernatant was used for Immunoprecipitation experiments. The cleared lysates was diluted 10 fold in dilution buffer (150 mM NaCl, 50 mM HEPES and 5mM EDTA and 1x protease inhibitor cocktail), and then incubated with anti-GFP magnetic agarose beads (Chromotek) at 4 °C for 120 min on a rotory shaker. The beads were then washed thrice with wash buffer (150 mM NaCl, 50 mM HEPES and 5mM EDTA). To pull down the immunocomplexes, beads were boiled in 30 μl of 2× SDS- PAGE sample buffer for 15 mins. The immunoprecipitated proteins were separated by SDS-PAGE. Western blot analysis was performed as previously described.

Data availability
The raw data that support the findings of this study are available from the corresponding author upon reasonable request.

Mass spectrometry raw data
Mass spectrometry raw data are available via ProteomeXchange with identifier PXD007761.

References

30. Tighe, A., Staples, O. & Taylor, S. Mps1 kinase activity restrains anaphase during an unperturbed mitosis and targets Mad2 to kinetochores. *J. Cell Biol.*

181, 893–901 (2008).
31. Paul, F. E., Hosp, F. & Selbach, M. Analyzing protein-protein interactions by quantitative mass spectrometry. *Methods* **54,** 387–395 (2011).
32. Rappsilber, J., Ishihama, Y. & Mann, M. Stop And Go Extraction tips for matrix-assisted laser desorption/ionization, nanoelectrospray, and LC/MS sample pretreatment in proteomics. *Anal. Chem.* **75,** 663–670 (2003).
33. Cox, J. & Mann, M. MaxQuant enables high peptide identification rates, individualized p.p.b.-range mass accuracies and proteome-wide protein quantification. *Nat. Biotechnol.* **26,** 1367–1372 (2008).
34. Cox, J. *et al.* Andromeda: A peptide search engine integrated into the MaxQuant environment. *J. Proteome Res.* **10,** 1794–1805 (2011).
35. Binns, D. *et al.* QuickGO: A web-based tool for Gene Ontology searching. *Bioinformatics* **25,** 3045–3046 (2009).
36. Aulas, A. & Vande Velde, C. Alterations in stress granule dynamics driven by TDP-43 and FUS: a link to pathological inclusions in ALS? *Front. Cell. Neurosci.* **9,** (2015).
37. Olsen, J. V. *et al.* Quantitative Phosphoproteomics Reveals Widespread Full Phosphorylation Site Occupancy During Mitosis. *Sci. Signal.* **3,** ra3-ra3 (2010).
38. Olsen, J. V. *et al.* Global, In Vivo, and Site-Specific Phosphorylation Dynamics in Signaling Networks. *Cell* **127,** 635–648 (2006).
39. Wootton, J. C., and Federhen, S. Analysis of compositionally biased regions in sequence databases. *Methods Enzym.* **266,** 554–571 (1996).
40. Cheng, C. & Sharp, P. A. Regulation of CD44 alternative splicing by SRm160 and its potential role in tumor cell invasion. *Mol. Cell. Biol.* **26,** 362–70 (2006).
41. Belin, B. J., Cimini, B. A., Blackburn, E. H. & Mullins, R. D. Visualization of actin filaments and monomers in somatic cell nuclei. *Mol. Biol. Cell* **24,** 982–994 (2013).
42. Bindels, D. S. *et al.* mScarlet: a bright monomeric red fluorescent protein for cellular imaging. *Nat. Methods* **14,** 53–56 (2016).
43. Pfleger, C. M., Lee, E. & Kirschner, M. W. Substrate recognition by the Cdc20 and Cdh1 components of the anaphase-promoting complex. *Genes Dev.* **15,** 2396–2407 (2001).
44. Jain, A. & Vale, R. D. RNA phase transitions in repeat expansion disorders. *Nature* **546,** 243–247 (2017).
45. Carpenter, A. E. *et al.* CellProfiler: Image analysis software for identifying and quantifying cell phenotypes. *Genome Biol.* **7,** (2006).
46. Rämö, P., Sacher, R., Snijder, B., Begemann, B. & Pelkmans, L. CellClassifier: Supervised learning of cellular phenotypes. *Bioinformatics* **25,** 3028–3030 (2009).
47. Jiang, H. *et al.* A Microtubule-Associated Zinc Finger Protein, BuGZ, Regulates Mitotic Chromosome Alignment by Ensuring Bub3 Stability and Kinetochore Targeting. *Dev. Cell* **28,** 268–281 (2014).

Figure Legends (Extended Data)

Extended data Figure 1. DYRK3 interactions are differentially regulated upon GSK-626616 treatment

a
Experimental design of SILAC quantitative pull-down assays to identify protein-protein interaction partners of DYRK3.
b
Experimental design of triple-SILAC quantitative pull-down assays to identify changes of DYRK3 interactors upon GSK-626616 inhibitor treatment.
c
Scatter plot shows changes of DYRK3 interactors upon GSK-626616 inhibitor treatment (normalized H/M $\log_2$ ratios). Only proteins detected as DYRK3 specific interactors (normalized H/L or M/L $\log_2$ ratio > 1) were retained on this plot. Interactors are considered differentially regulated (colored rims) if the H/M $\log_2$ ratio is greater than 1 or less than -1.
d
Mean intensity of DYRK3 interactors upon GSK-626616 inhibitor treatment (representative of two technical replicates).
e
Protein abundance of DYRK3 interactors and DYRK3 upon GSK-626616 inhibitor treatment (representative of two independent experiments).

Box plots: central mark: population median; box: interquartile range; whiskers: 1st/3rd quartile ± 1.5* interquartile range; outliers: dots.

Extended data Figure 2. GSK-626616 inhibited DYRK3 localizes to stress granules and forms mitotic granules

a
Western blot shows expression level of endogenous DYRK3 and GFP-DYRK3 in HeLa Flp-In T-Rex cells stably expressing inducible GFP-wildtype DYRK3. GFP-DYRK3 expression was induced by doxycycline (500ng/mL, 4hrs). Same induction conditions were used for Fig. 1c-e and Extended data 2b).

b
Colocalization of GSK-626616 inhibited (1μM, 2hrs) GFP-wildtype DYRK3 with stress granules upon arsenite treatment (500μM, 45mins).

c
Mitotic cells show formation of small DYRK3-positive granules upon GSK-626616 treatment (1μM, 1hr).

d
Phosphoproteomic data of human cell cycle showing changes of regulated phospho-sites that are associated with DYRK3 specific interactors detected in Fig. 1a. The majority (74.4%) of these phospho-sites reached peak level at mitosis. The phospho-site occupancy level is displayed for those sites that were downregulated upon GSK-626616 inhibitor treatment as reported in Wippich, et al. 2013. The phosphoproteomic data were retrieved from Olsen, et al. 2010. The known localization (splicing speckle, stress granule or centrosome) of the corresponding protein is indicated for each phospho-site.

Images and western blot are representative of at least three independent experiments. Scale bars: 10 μm.

Extended data Figure 3. DYRK3 inhibition forms aberrant mitotic granules

a
Dissolved staining of splicing speckle marker (SC35) in mitotic cells upon DMSO treatment.
b
Dissolved staining of stress granule marker (PABP) in mitotic cells upon DMSO treatment**.**
c
Spindle pole localization of pericentriolar material protein (PCM1) in mitotic cells upon DMSO treatment.
d
Mitotic cells (HEK293T) show formation of SC35 granules upon GSK-626616 treatment (1μM, 1hr).
e
Formation of SON granules in mitotic cells upon GSK-626616 treatment (1μM, 6hr).
f
Formation of TIAR granules in mitotic cells upon GSK-626616 treatment (1μM, 6hr).
g
Left: Quantification of fraction of mitotic (metaphase) cells with SC35 granules on treatment with kinase inhibitors (1μM, 1hr).
Right: Quantification of fraction of mitotic (metaphase) cells with PABP granules on treatment with kinase inhibitors (1μM, 3hr).
Inhibitors and the corresponding kinase targets are mentioned. Data are Mean ± SD (n=3 technical replicates)

Images are representative of at least three independent experiments. Scale bars: 10 μm.

Extended data Figure 4. Formation of mitotic granules is DYRK3 specific

a
Mitotic cells show no colocalization between splicing speckle marker (SC35) and SRPK1 upon GSK-626616 treatment (1μM, 1hr).
b
Mitotic cells show no colocalization between splicing speckle marker (SC35) and CYCLIN B upon GSK-626616 treatment (1μM, 1hr).
c
Mitotic cells show no colocalization between splicing speckle marker (SRRM2) and CDK1 upon GSK-626616 treatment (1μM, 1hr).
d
Mitotic cells stained for pY15 CDK1. Loss of pY15 signal (CDK1 activation) in mitotic cells upon GSK-626616 (1μM, 1hr) treatment is comparable to DMSO control.
e
GSK-626616 treatment (1μM, 1hr) does not result in decrease in pT446 APC3 (CDK1 mitotic substrate) signal in mitotic cells compared to DMSO control.
f
Mitotic cells show staining for pT446 APC3 (CDK1 mitotic substrate). The cells were pre-permeabilized with Triton-X before fixation. pT446 APC3 signal can be observed at spindle poles for both DMSO and GSK-626616 treatment (1μM, 1hr).
g
Appearance of SC35 granules and spindle apparatus defects upon DYRK3 knockdown.
Right: Quantification of SC35 granule number in mitotic (metaphase) cells (4 independent experiments).

Box plots: central mark: population median; box: interquartile range; whiskers: 1st/3rd quartile ± 1.5* interquartile range; outliers: dots. Statistical analysis performed across cells by Welch two-sided t-test.

Images and data are representative of at least three independent experiments. Scale bars: 10 μm.

Extended data Figure 5. Inhibition of DYRK3 does not affect all membrane-less organelles in mitosis

a
Colocalization of splicing marker and Poly(A) mRNA in hybrid compartments in mitotic cells upon GSK-626616 treatment (1μM, 3hr)
b
Colocalization of splicing marker and GFP-wildtype DYRK3 in hybrid compartments in mitotic cells upon GSK-626616 treatment (1μM, 2hrs)
c
Dissolution of P-bodies (DDX6) in mitotic cells is unaffected upon GSK-626616 treatment (1μM, 6hrs).
d
Dissolution of nucleoli (Fibrillarin) in mitotic cells is unaffected upon GSK-626616 treatment (1μM, 6hrs).
e
Dissolution of Cajal bodies (Coilin) in mitotic cells is unaffected upon GSK-626616 treatment (1μM, 6hrs).
f
Aberrant granules formed upon GSK-626616 treatment are not ubiquitinated aggregates.

Images and data are representative of at least three independent experiments. Scale bars: 10 μm.

Extended data Figure 6. Protein abundance does not change during formation of mitotic granule upon GSK-626616 inhibitor treatment

a
Time-lapse images (single Z-stack) show fusion of mitotic SRRM2-mCherry granules formed in the presence of GSK-626616 inhibitor (1μM) in cells arrested in mitosis (thymidine-nocodazole block).
b
Mean cell intensity of SRRM2-mCherry is plotted during mitotic granule formation on addition of GSK-626616 inhibitor (1μM). Data are Mean ± SD.
c
Top: Mean intensity of SRRM2-mCherry in the dissolved phase is plotted during mitotic granule formation on addition of GSK-626616 inhibitor (1μM).
Bottom: Time-lapse images of the cells plotted in the top panel.

Images are representative of at least three independent experiments. Scale bars: 10 μm.

Extended data Figure 7. Dissolution of membrane-less organelles is dependent on DYRK3 localization and its kinase activity

a
Images show cells overexpressing GFP-wildtype (WT) and kinase-dead (K218M) DYRK3. These images are the same as Fig. 3a showing both channels.
b
Dissolution of splicing speckles upon overexpressing GFP-wildtype (WT) DYRK3 in interphase cells is reversed by GSK-626616 treatment (1μM, 2hrs).
c
Top: Schematic representation of GFP-tagged NLS (Nuclear Localizing Signal) mutant of DYRK3. Arginine (R) and Lysine (K) residues in the NLS are mutated to Alanine (A).
Bottom: Overexpressed GFP-tagged NLS mutant of DYRK3 localizes to the cytoplasm and does not dissolve splicing speckles.
d
Left: Dissolution of splicing speckles upon overexpressing GFP- NLS (SV40) tagged wildtype (WT) DYRK3 in interphase cells.
Middle: Dissolution of splicing speckles upon overexpressing GFP- NLS (SV40) tagged wildtype (WT) DYRK3 in interphase cells is reversed upon GSK-626616 treatment (1μM, 2hrs).
Right: Condensed splicing speckles upon overexpressing GFP- NLS (SV40) tagged kinase-dead (K218M) DYRK3 in interphase cells.
e
Images show cells overexpressing GFP-wildtype (WT) and kinase-dead (K218M) DYRK3. These images are the same as Fig. 3c showing both channels.
f
Dissolution of pericentriolar satellites upon overexpressing GFP-wildtype (WT) DYRK3 in interphase cells is reversed upon GSK-626616 treatment (1μM, 2hrs).
g
Images show cells overexpressing GFP-wildtype (WT) and kinase-dead (K218M) DYRK3. These images are the same as Fig. 3e showing both channels.
h
Dissolution of stress granules upon overexpressing GFP-wildtype (WT) DYRK3 in interphase cells is reversed upon GSK-626616 treatment (1μM, 2hrs).
i
The percentage of low complexity regions (LCR) occupying each full-length protein was computed for all DYRK3 interactors (Fig. 1a) and all the known splicing speckle components (GO:0016607). SRRM1 shown in blue is among the proteins with the highest proportion of low complexity regions.
j
Dissolution of GFP-PCM1(1-1468) cytosolic granules upon overexpressing RFP-wildtype (WT) DYRK3, and not kinase-dead (K218M) DYRK3.
k
Time-lapse images show RFP-wildtype (WT) DYRK3 driven dissolution of cytosolic granules formed upon GFP-PCM1(1-1468) overexpression.

l
Dissolution of mCherry-SRRM1 nuclear granules upon overexpressing GFP-wildtype (WT) DYRK3, and not kinase-dead (K218M) DYRK3.

m
Nucleoli are unaffected upon overexpressing GFP-wildtype (WT) DYRK3 or kinase-dead (K218M) DYRK3 in interphase cells.

Images are representative of at least three independent experiments. All scale bars: 10 μm.

Extended data Figure 8. Dilution of DYRK3 substrates during G2 to M transition

a
Top: Time-lapse images of a cell (single Z-stack) expressing GFP-3xNLS (Nuclear Localizing Signal) during G2 to M transition.
Bottom: Changes in mean nuclear intensity of GFP-3xNLS during G2 to M transition. The lines (background) show mean nuclear intensity for individual cells (n=11). Data are Mean ± SD. Time point (0 min) refers to nuclear envelope breakdown.
b
Top: Time-lapse images of a cell (single Z-stack) expressing pmScarlet-NES (Nuclear Export Signal) during G2 to M transition.
Bottom: Changes in mean cytoplasmic intensity of pmScarlet-NES during G2 to M transition. The lines (background) show mean nuclear intensity for individual cells (n=8). Data are Mean ± SD. Time point (0 min) refers to nuclear envelope breakdown.
c
Top: Time-lapse images of a cell (single Z-stack) expressing GFP-wildtype DYRK3 during G2 to M transition.
Bottom: Changes in mean cytoplasmic intensity of GFP-wildtype DYRK3 during G2 to M transition. The lines (background) show mean cytoplasmic intensity for individual cells (n=9). Data are Mean ± SD. Time point (0 min) refers to nuclear envelope breakdown.
d
Top: Time-lapse images of a cell (single Z-stack) expressing GFP-PCM1(1-1468) during G2 to M transition.
Bottom: Changes in mean cytoplasmic intensity of GFP-PCM1(1-1468) during G2 to M transition. The lines (background) show mean nuclear intensity for individual cells (n=11). Data are Mean ± SD. Time point (0 min) refers to nuclear envelope breakdown.
e
Overexpressing mCherry-SRRM1 form mitotic granules which recruit endogenous splicing proteins.
f
Time-lapse images (single Z-stack) show fusion of mitotic mCherry-SRRM1 granules in mitotic cells.
g
Left: FRAP analysis of interphase and mitotic mCherry-SRRM1 granules in the presence and absence of GSK-626616 inhibitor (1μM). Data are Mean ± SD.
Right: FRAP recovery of mitotic mCherry-SRRM1 granule.
h
Cells arrested in mitosis show formation of splicing granules upon GSK-626616 treatment (1μM, indicated times).
Data and images are representative of at least three independent experiments. Scale bars: 10 μm.

Extended data Figure 9. Spindle apparatus defects upon DYRK3 inhibition

a
Multiple γ-tubulin foci in mitotic cells upon GSK-626616 treatment (1μM, 6hr).
b
Top: ZNF207 localization in interphase cells (No pre-permeabilization).
Bottom: ZNF207 and SC35 colocalize in Triton-X pre-permeabilized interphase cells.
c
ZNF207 granules in mitotic cells upon GSK-626616 treatment (1μM, 3hr).
d
GFP-wildtype (WT) DYRK3 colocalizes with ZNF207 in mitotic cells upon GSK-626616 treatment (1μM, 3hr). GFP-wildtype DYRK3 expression was induced in HeLa Flp-In T-Rex cells by adding doxycycline (500ng/mL, 6hrs).

Images are representative of at least three independent experiments. Scale bars: 10 μm.

Extended data Figure 10. DYRK3 forms ubiquitin-positive aggregates on overexpression of Cdc20 and Cdh1 or upon proteosomal inhibition

a
Ubiquitin does not colocalize with overexpressed GFP inside cells.
b
Ubiquitin localizes to GFP-wildtype DYRK3 aggregates, formed on HA-Cdh1 and HA-Cdc20 overexpression.
c
Ubiquitin does not colocalize with overexpressed GFP upon MG-132 treatment (5μM, 4hrs).
d
Ubiquitin localizes to GFP-wildtype DYRK3 granules upon MG-132 treatment (5μM, 4hrs). GFP-wildtype DYRK3 expression was induced in HeLa Flp-In T-Rex cells by adding doxycycline (500ng/mL, 6hrs).
e
Top: GFP-wildtype DYRK3 overexpression prevents re-assembly of cytosolic mCherry-SRRM1 granules during late mitosis.
Bottom: GFP-wildtype DYRK3 overexpression prevents re-assembly of cytosolic splicing granules during late mitosis.

Images are representative of at least three independent experiments. Scale bars: 10 μm

Figure 1

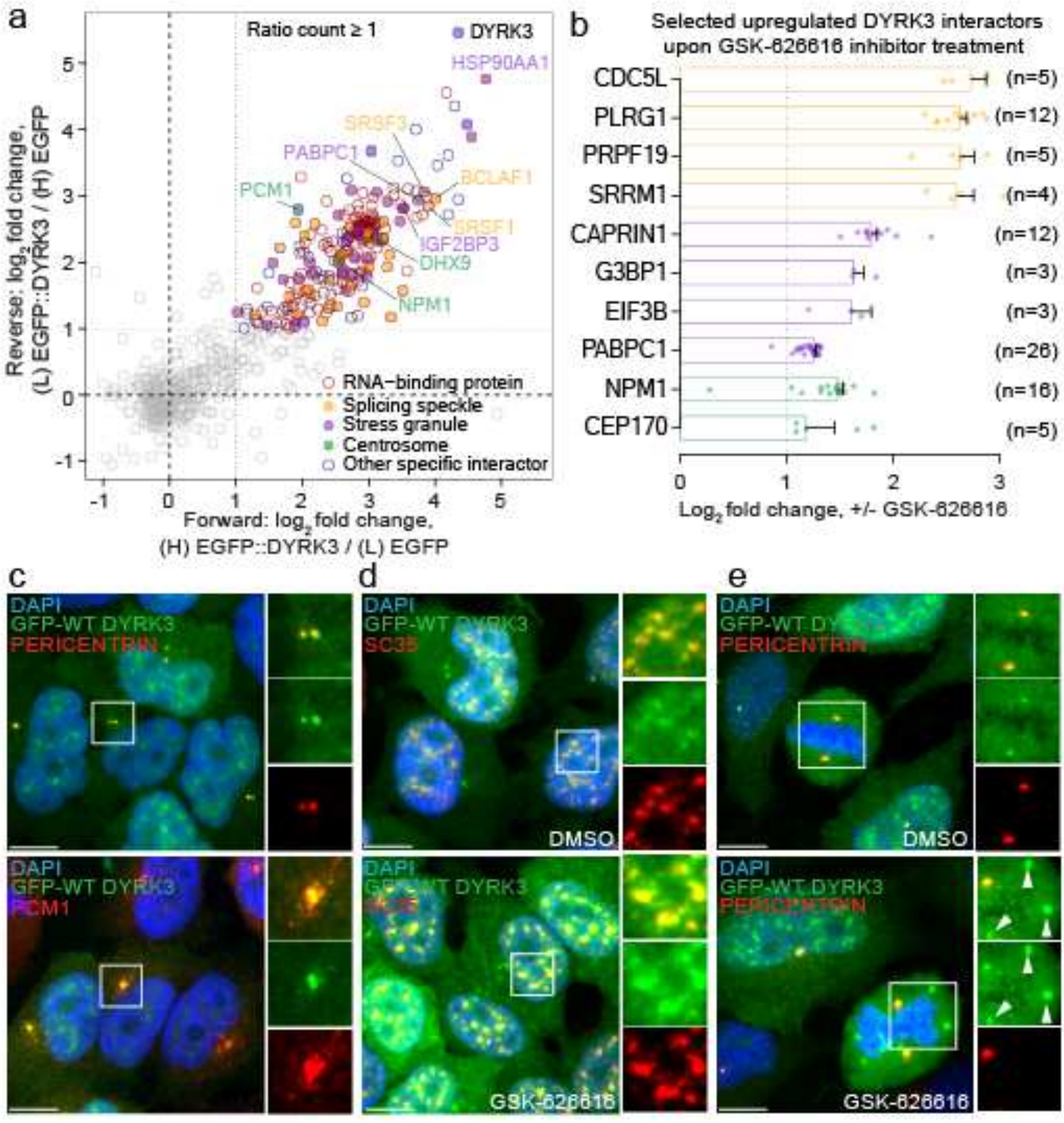
a
Ratio count ≥ 1
DYRK3
HSP90AA1
SRSF3
PABPC1
PCM1
BCLAF1
SRSF1
IGF2BP3
DHX9
NPM1
RNA−binding protein
Splicing speckle
Stress granule
Centrosome
Other specific interactor
Reverse: log2 fold change, (L) EGFP::DYRK3 / (H) EGFP
Forward: log2 fold change, (H) EGFP::DYRK3 / (L) EGFP
b
Selected upregulated DYRK3 interactors upon GSK-626616 inhibitor treatment
CDC5L (n=5)
PLRG1 (n=12)
PRPF19 (n=5)
SRRM1 (n=4)
CAPRIN1 (n=12)
G3BP1 (n=3)
EIF3B (n=3)
PABPC1 (n=26)
NPM1 (n=16)
CEP170 (n=5)
Log2 fold change, +/- GSK-626616
c
DAPI
GFP-WT DYRK3
PERICENTRIN
PCM1
d
SC35
DMSO
GSK-626616
e

Figure 2

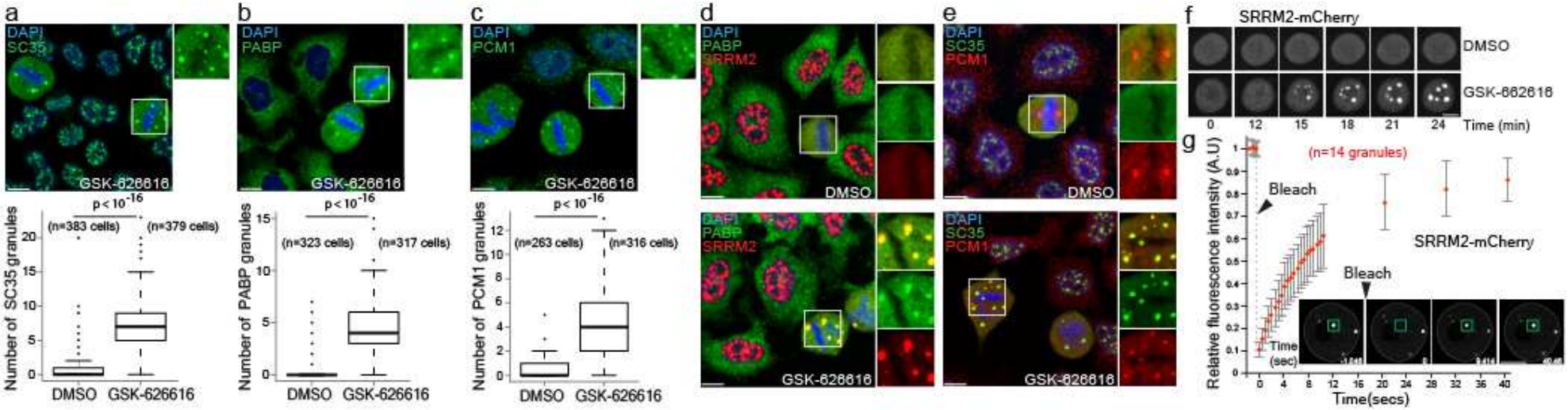
a
DAPI
SC35
GSK-626616
p < 10-16
(n=383 cells)
(n=379 cells)
Number of SC35 granules
DMSO
GSK-626616
b
DAPI
PABP
GSK-626616
p < 10-16
(n=323 cells)
(n=317 cells)
Number of PABP granules
DMSO
GSK-626616
c
DAPI
PCM1
GSK-626616
p < 10-16
(n=263 cells)
(n=316 cells)
Number of PCM1 granules
DMSO
GSK-626616
d
DAPI
PABP
SRRM2
DMSO
DAPI
PABP
SRRM2
GSK-626616
e
DAPI
SC35
PCM1
DMSO
DAPI
SC35
PCM1
GSK-626616
f
SRRM2-mCherry
DMSO
GSK-662616
0
12
15
18
21
24
Time (min)
g
(n=14 granules)
Bleach
SRRM2-mCherry
Bleach
Relative fluorescence intensity (A.U)
Time (sec)
Time(secs)

Figure 3

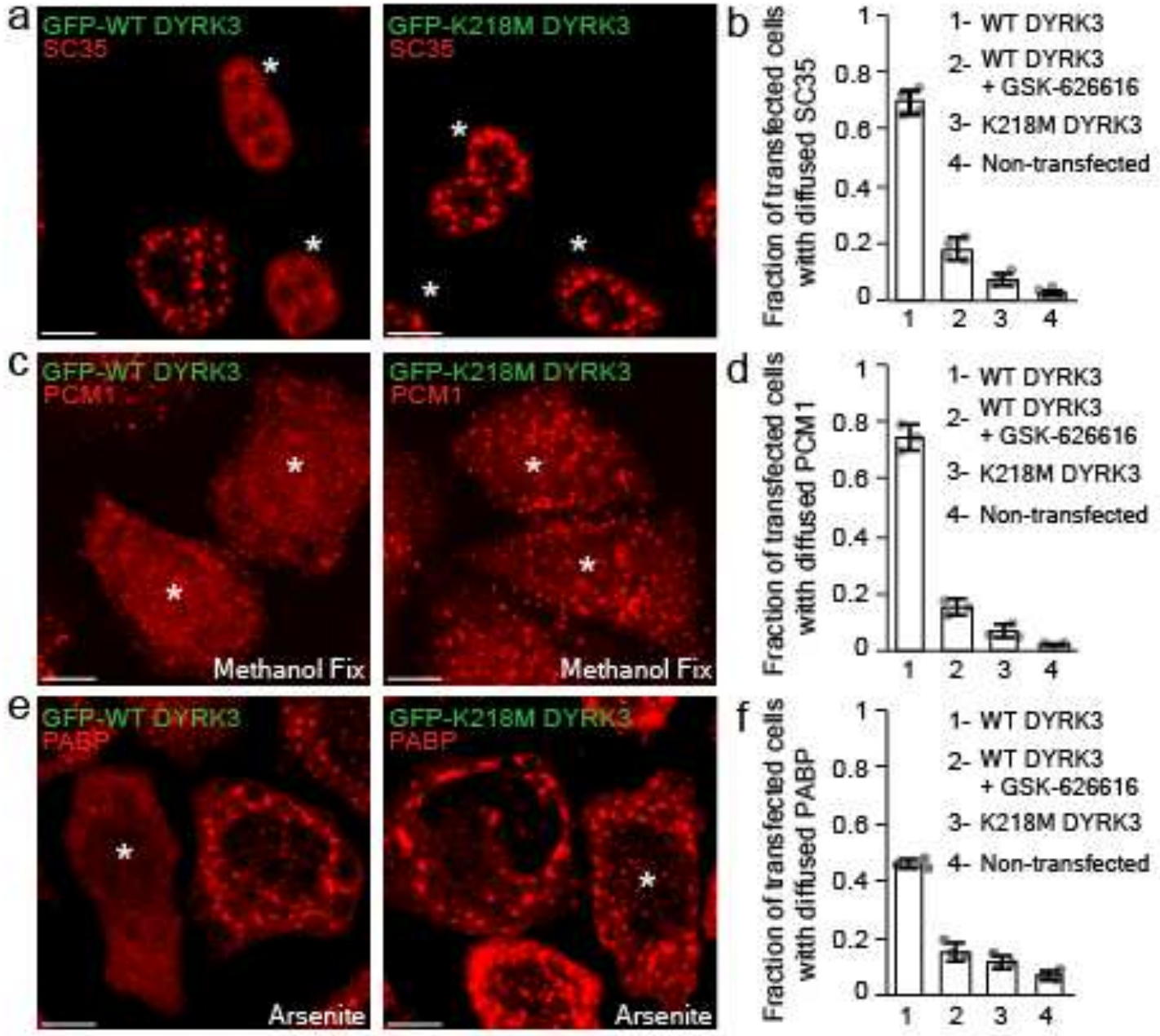
a
GFP-WT DYRK3
SC35
GFP-K218M DYRK3
SC35
b
Fraction of transfected cells with diffused SC35
1- WT DYRK3
2- WT DYRK3 + GSK-626616
3- K218M DYRK3
4- Non-transfected
c
GFP-WT DYRK3
PCM1
Methanol Fix
GFP-K218M DYRK3
PCM1
Methanol Fix
d
Fraction of transfected cells with diffused PCM1
1- WT DYRK3
2- WT DYRK3 + GSK-626616
3- K218M DYRK3
4- Non-transfected
e
GFP-WT DYRK3
PABP
Arsenite
GFP-K218M DYRK3
PABP
Arsenite
f
Fraction of transfected cells with diffused PABP
1- WT DYRK3
2- WT DYRK3 + GSK-626616
3- K218M DYRK3
4- Non-transfected

Figure 4

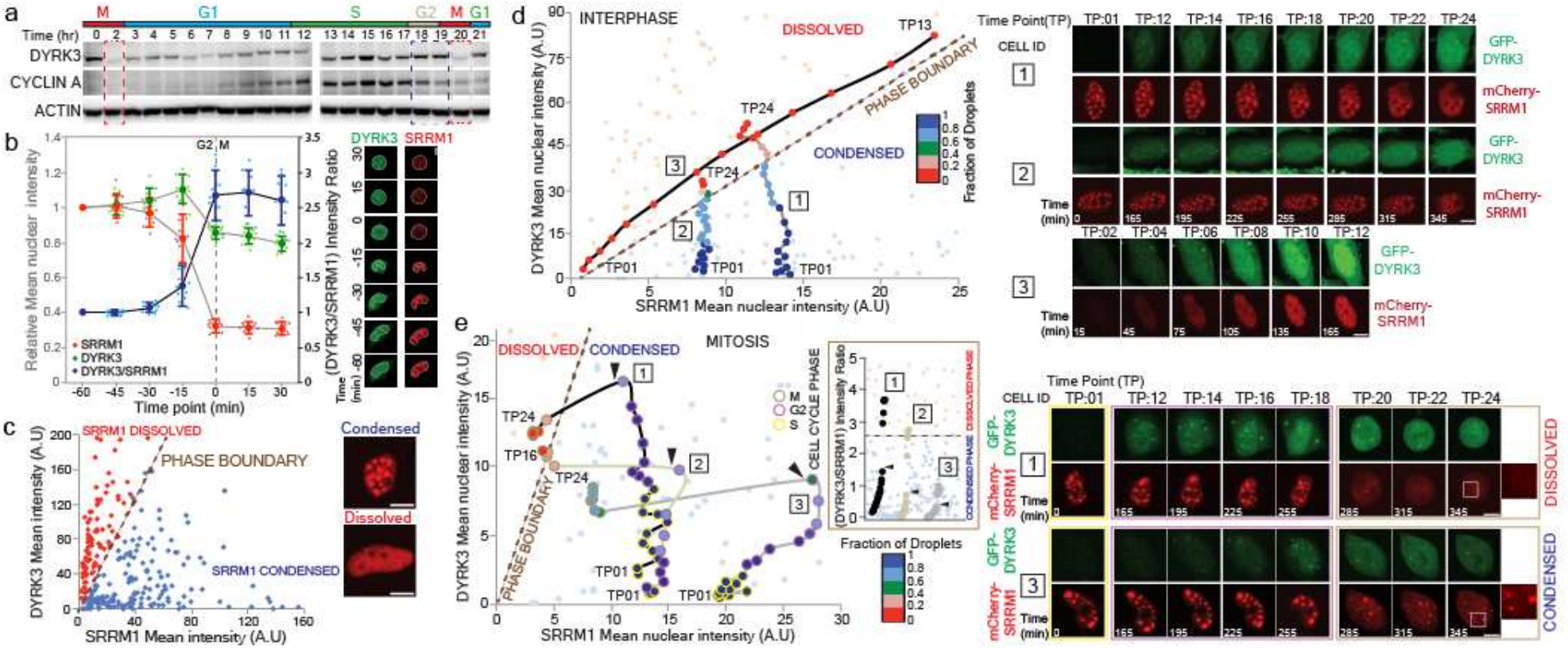
a
M
G1
S
G2
M
G1
Time (hr)
DYRK3
CYCLIN A
ACTIN
b
G2
M
Relative Mean nuclear intensity
(DYRK3/SRRM1) Intensity Ratio
Time point (min)
SRRM1
DYRK3
DYRK3/SRRM1
DYRK3
SRRM1
Time (min)
c
SRRM1 DISSOLVED
PHASE BOUNDARY
SRRM1 CONDENSED
DYRK3 Mean intensity (A.U)
SRRM1 Mean intensity (A.U)
Condensed
Dissolved
d
INTERPHASE
DISSOLVED
CONDENSED
PHASE BOUNDARY
TP13
TP24
TP01
Fraction of Droplets
DYRK3 Mean nuclear intensity (A.U)
SRRM1 Mean nuclear intensity (A.U)
Time Point(TP)
CELL ID
GFP-DYRK3
mCherry-SRRM1
Time (min)
e
MITOSIS
DISSOLVED
CONDENSED
PHASE BOUNDARY
TP24
TP16
TP01
M
G2
S
CELL CYCLE PHASE
(DYRK3/SRRM1) Intensity Ratio
Fraction of Droplets
DYRK3 Mean nuclear intensity (A.U)
SRRM1 Mean nuclear intensity (A.U)
Time Point (TP)
CELL ID
GFP-DYRK3
mCherry-SRRM1
Time (min)
DISSOLVED
CONDENSED

Figure 5

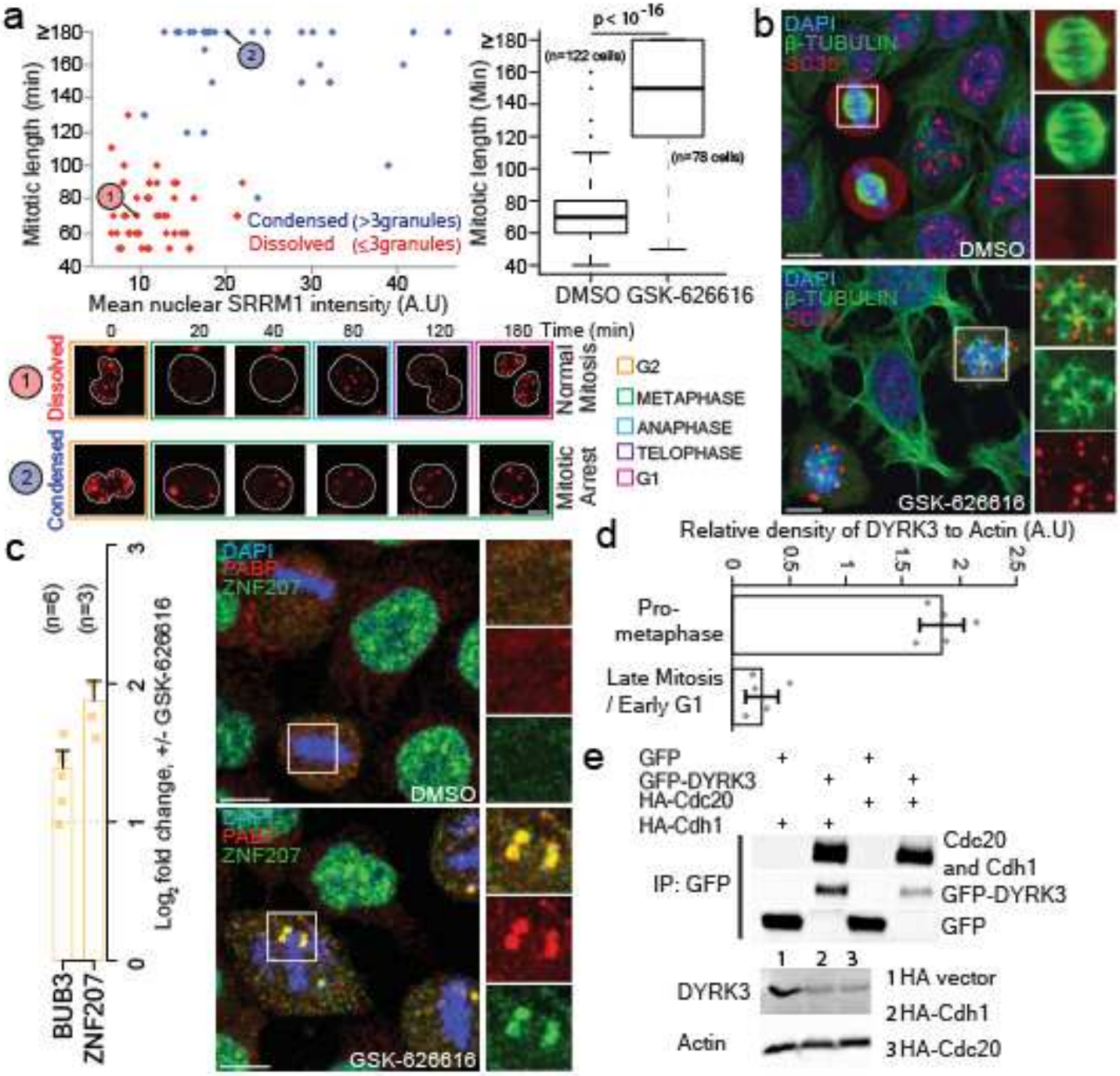
a
Mitotic length (min)
Mean nuclear SRRM1 intensity (A.U)
Condensed (>3granules)
Dissolved (≤3granules)
p< 10-16
(n=122 cells)
(n=78 cells)
Mitotic length (Min)
DMSO GSK-626616
Time (min)
Dissolved
Condensed
Normal Mitosis
Mitotic Arrest
G2
METAPHASE
ANAPHASE
TELOPHASE
G1
b
DAPI
β-TUBULIN
DMSO
GSK-626616
c
Log2 fold change, +/- GSK-626616
(n=6)
(n=3)
BUB3
ZNF207
DAPI
PABP
ZNF207
DMSO
GSK-626616
d
Relative density of DYRK3 to Actin (A.U)
Pro-metaphase
Late Mitosis / Early G1
e
GFP
GFP-DYRK3
HA-Cdc20
HA-Cdh1
IP: GFP
Cdc20 and Cdh1
GFP-DYRK3
GFP
DYRK3
Actin
1 HA vector
2 HA-Cdh1
3 HA-Cdc20

Figure 6

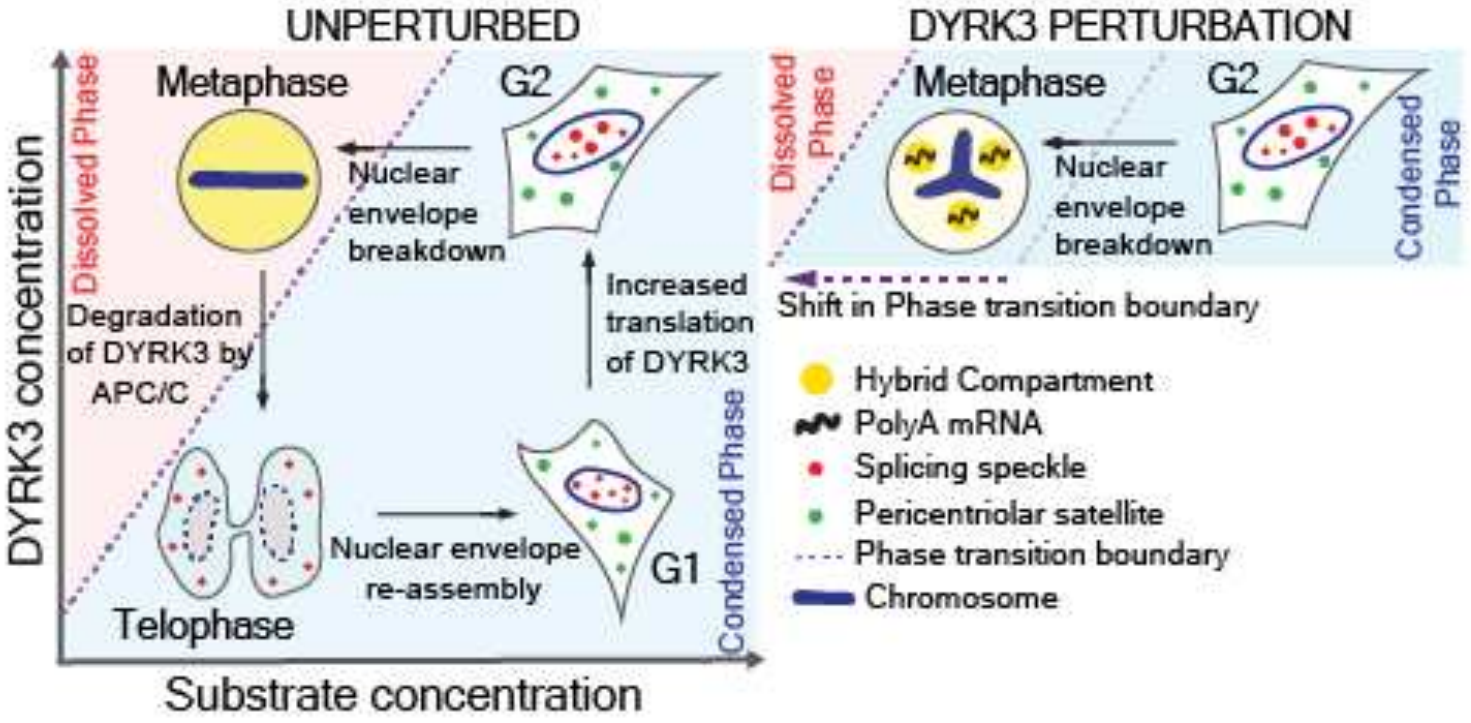
UNPERTURBED
DYRK3 PERTURBATION
Metaphase
G2
Nuclear envelope breakdown
Dissolved Phase
Condensed Phase
DYRK3 concentration
Degradation of DYRK3 by APC/C
Increased translation of DYRK3
Nuclear envelope re-assembly
G1
Telophase
Substrate concentration
Shift in Phase transition boundary
Hybrid Compartment
PolyA mRNA
Splicing speckle
Pericentriolar satellite
Phase transition boundary
Chromosome

Extended data 1

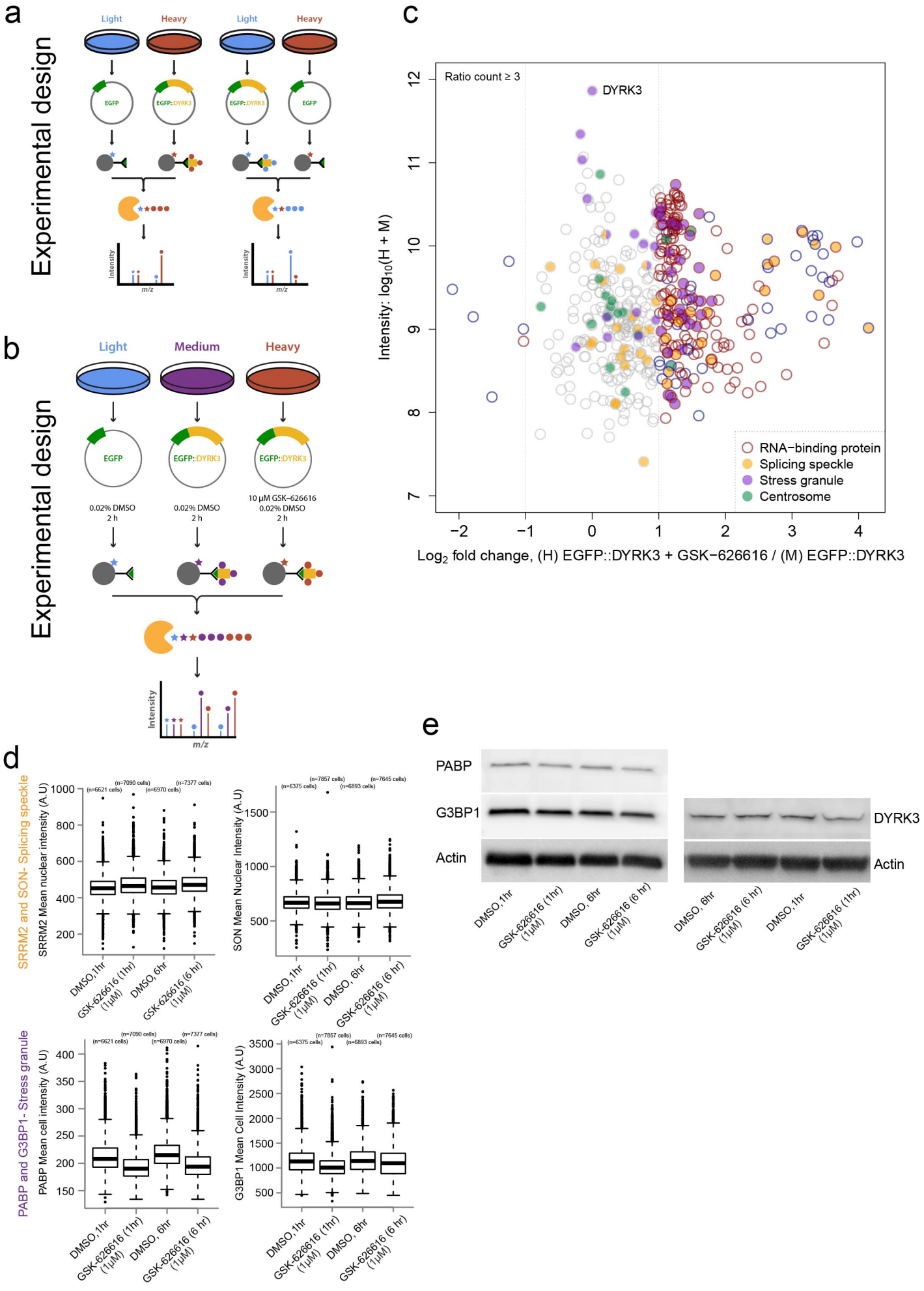

Extended data 2

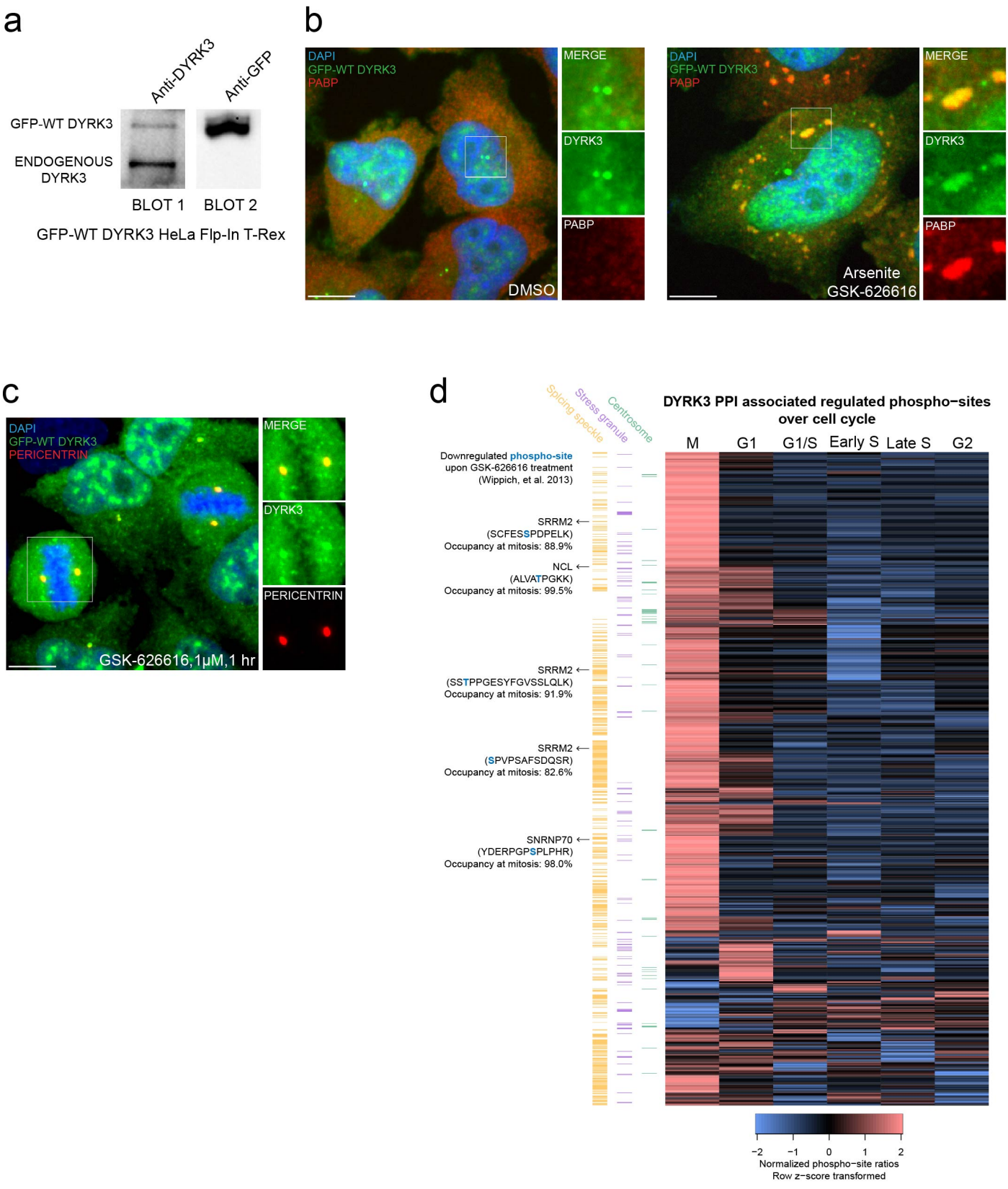

Extended data 3

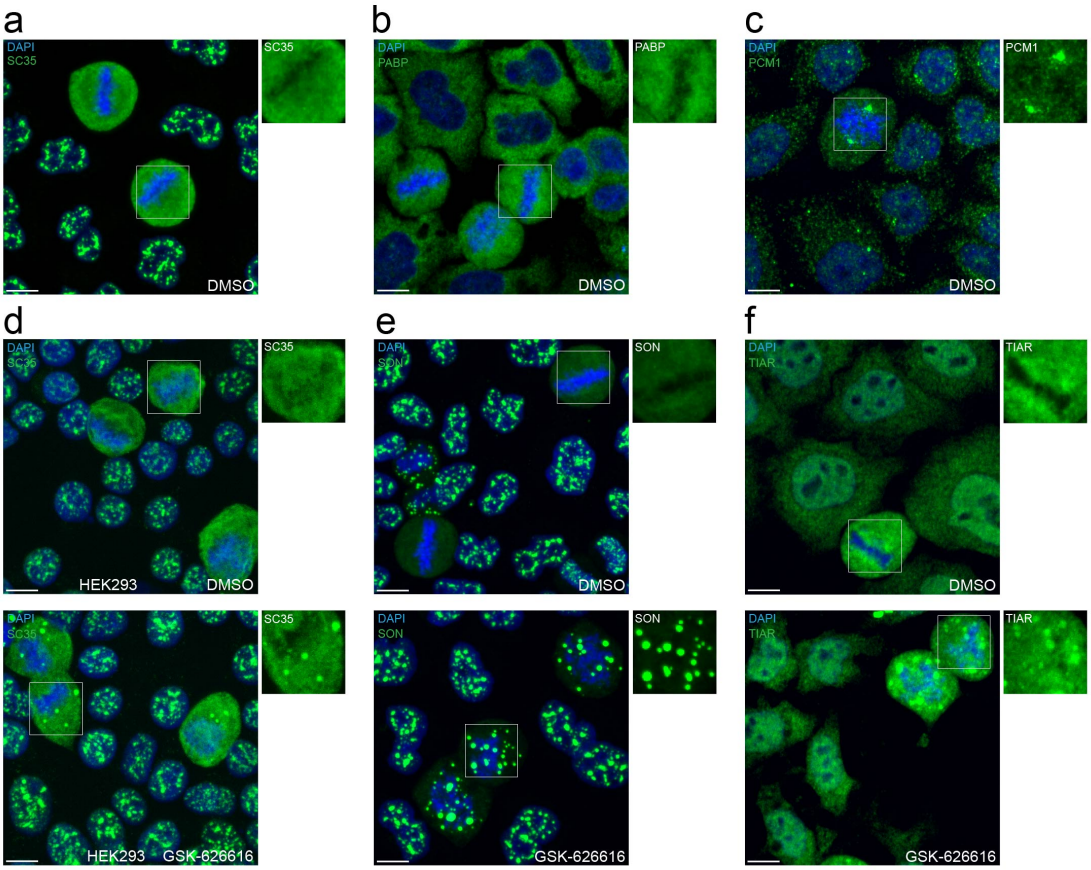

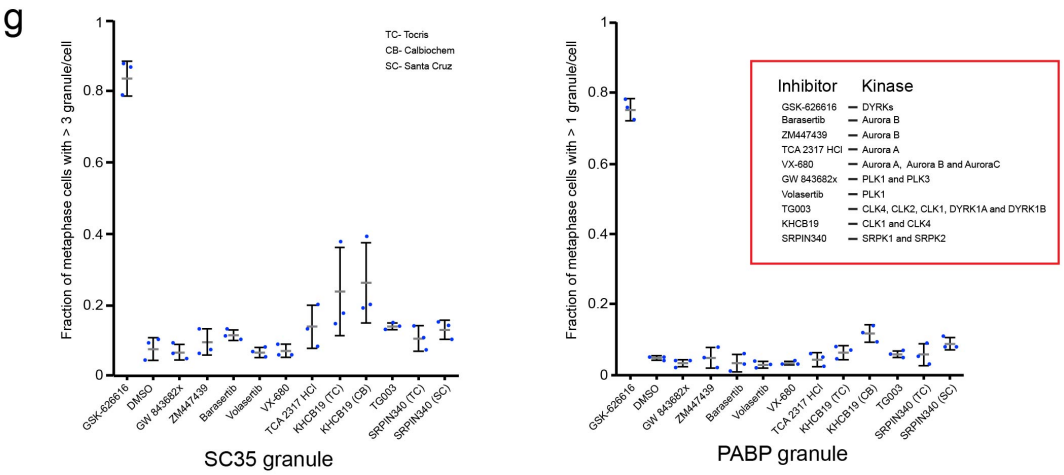

Extended data 4

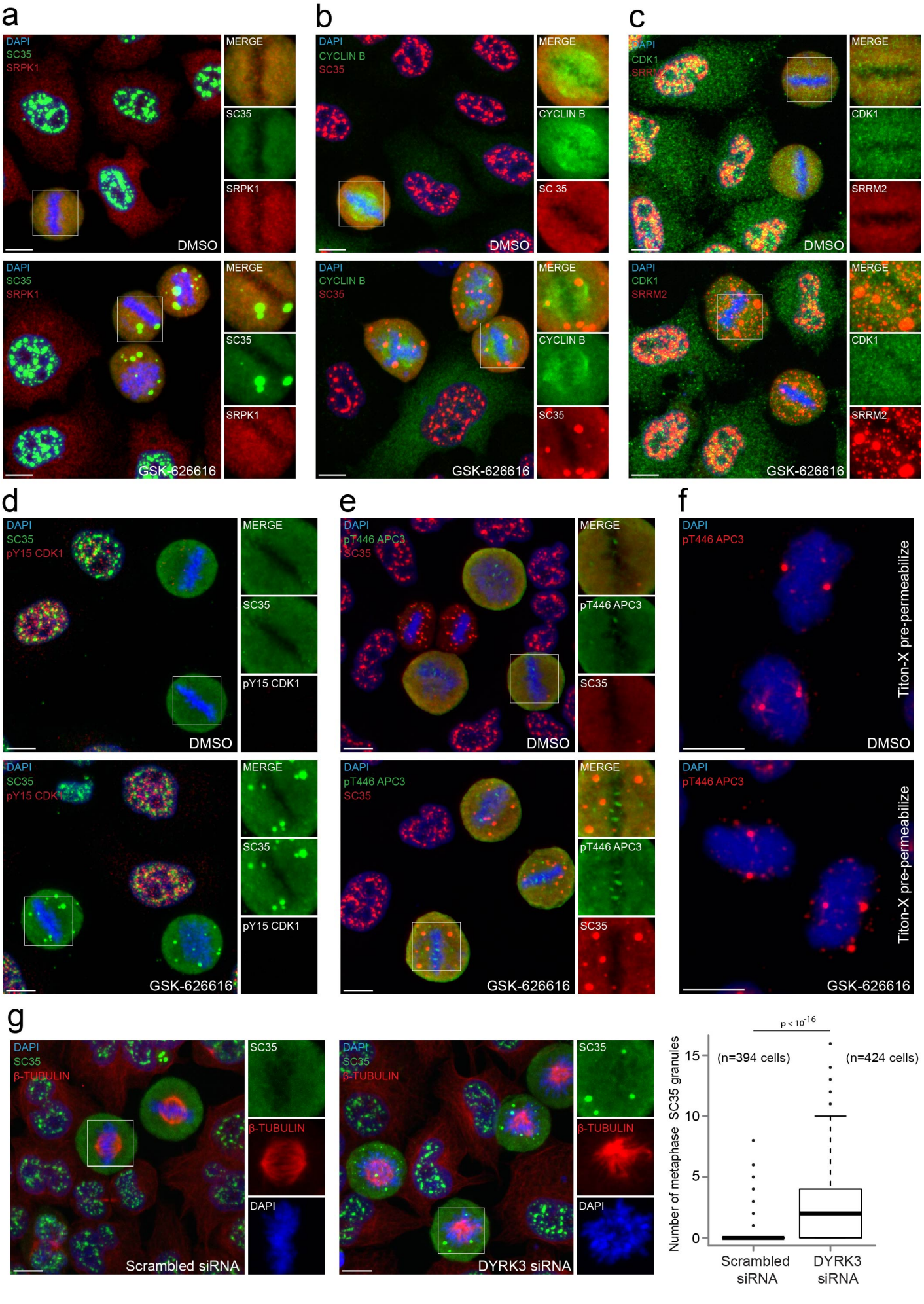

Extended data 5

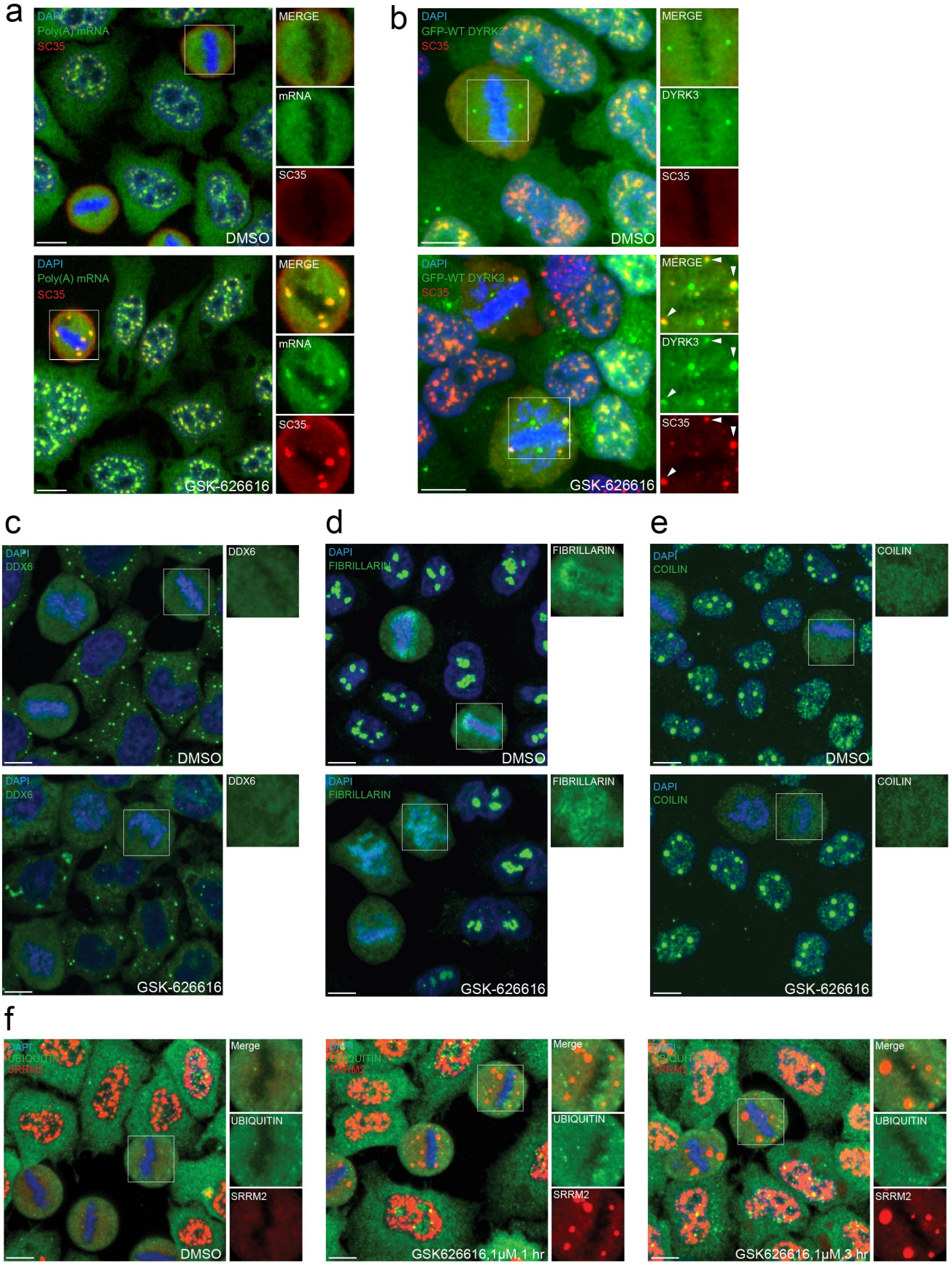

Extended data 6

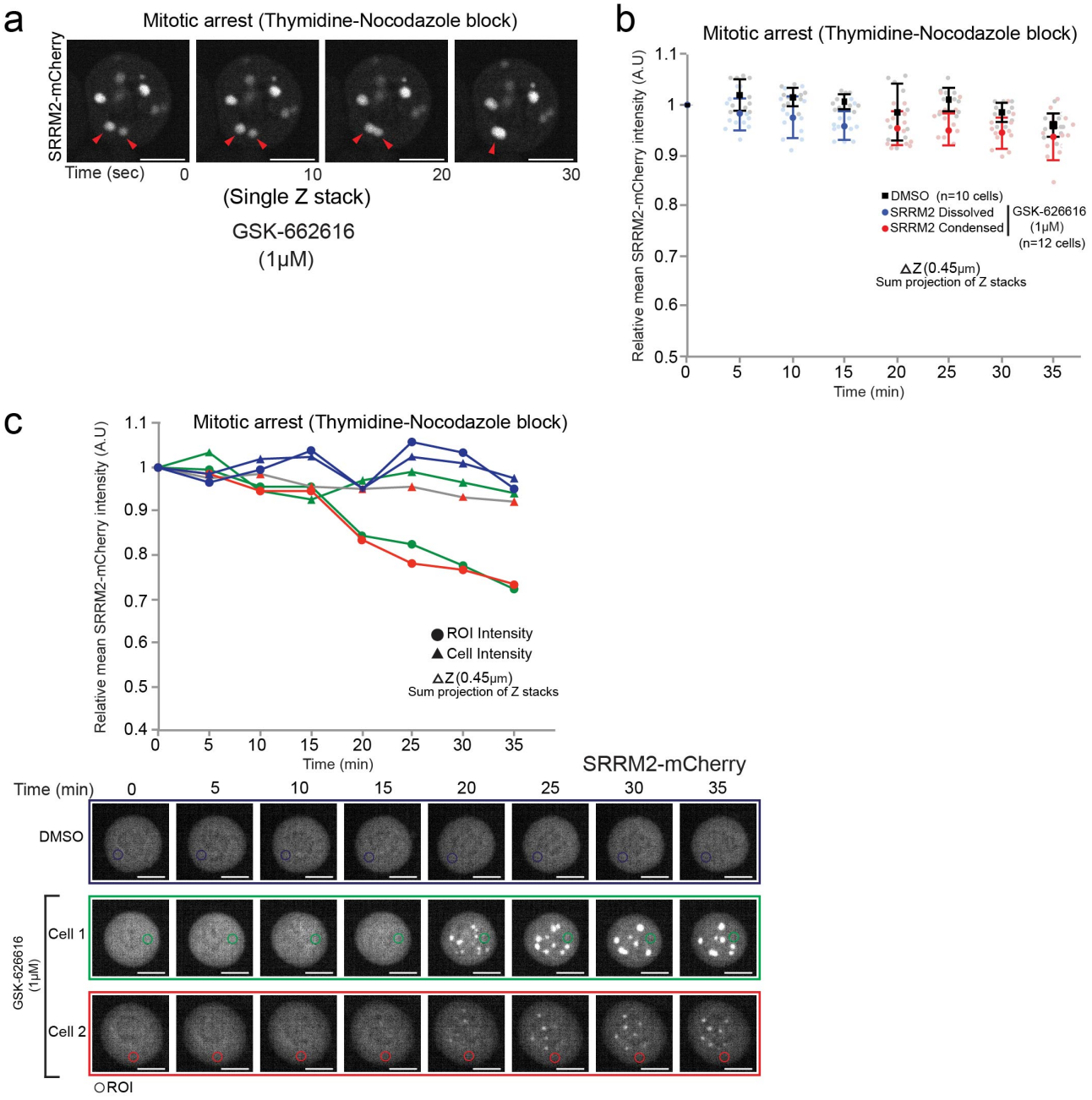

Extended data 7

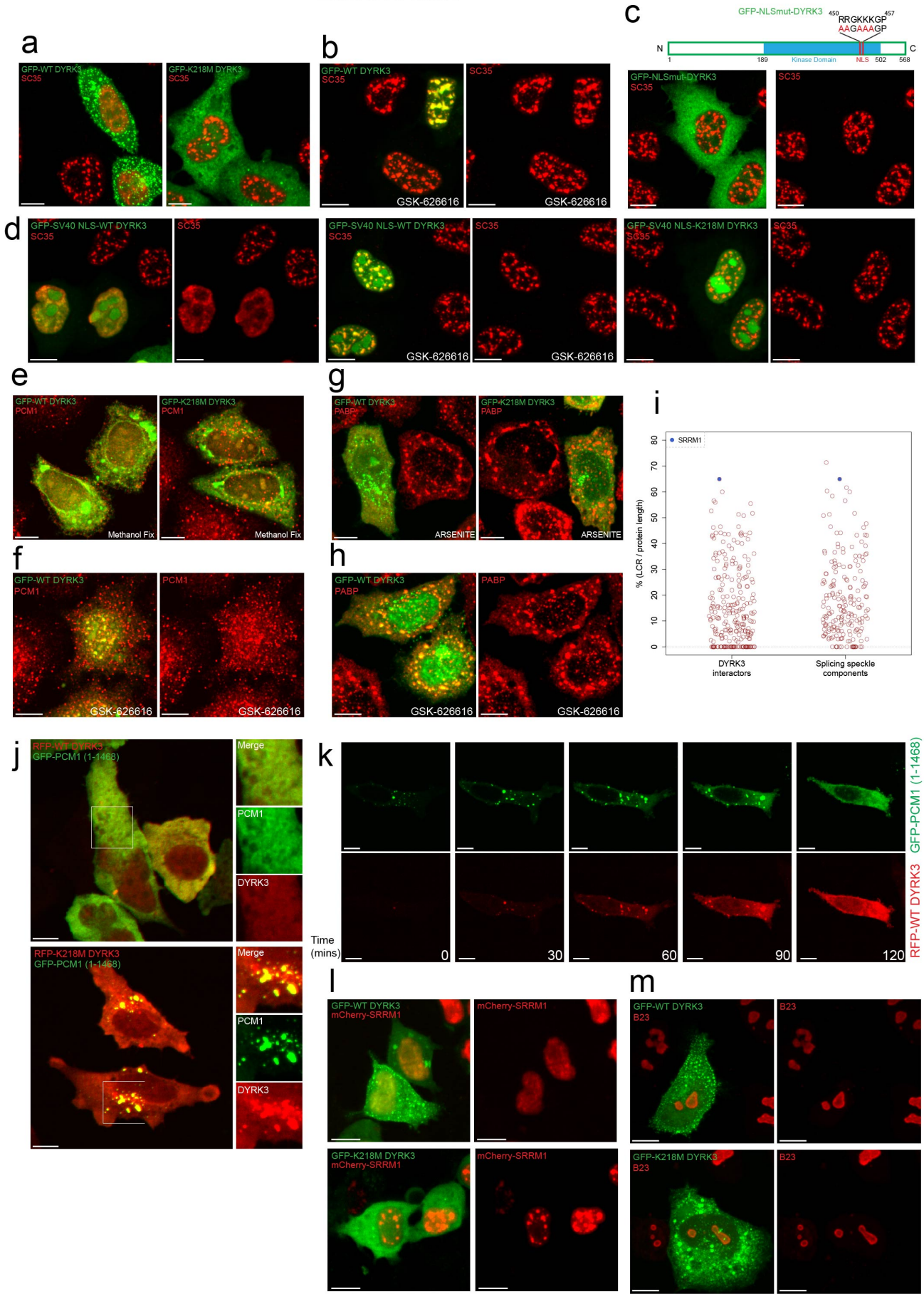

Extended data 8

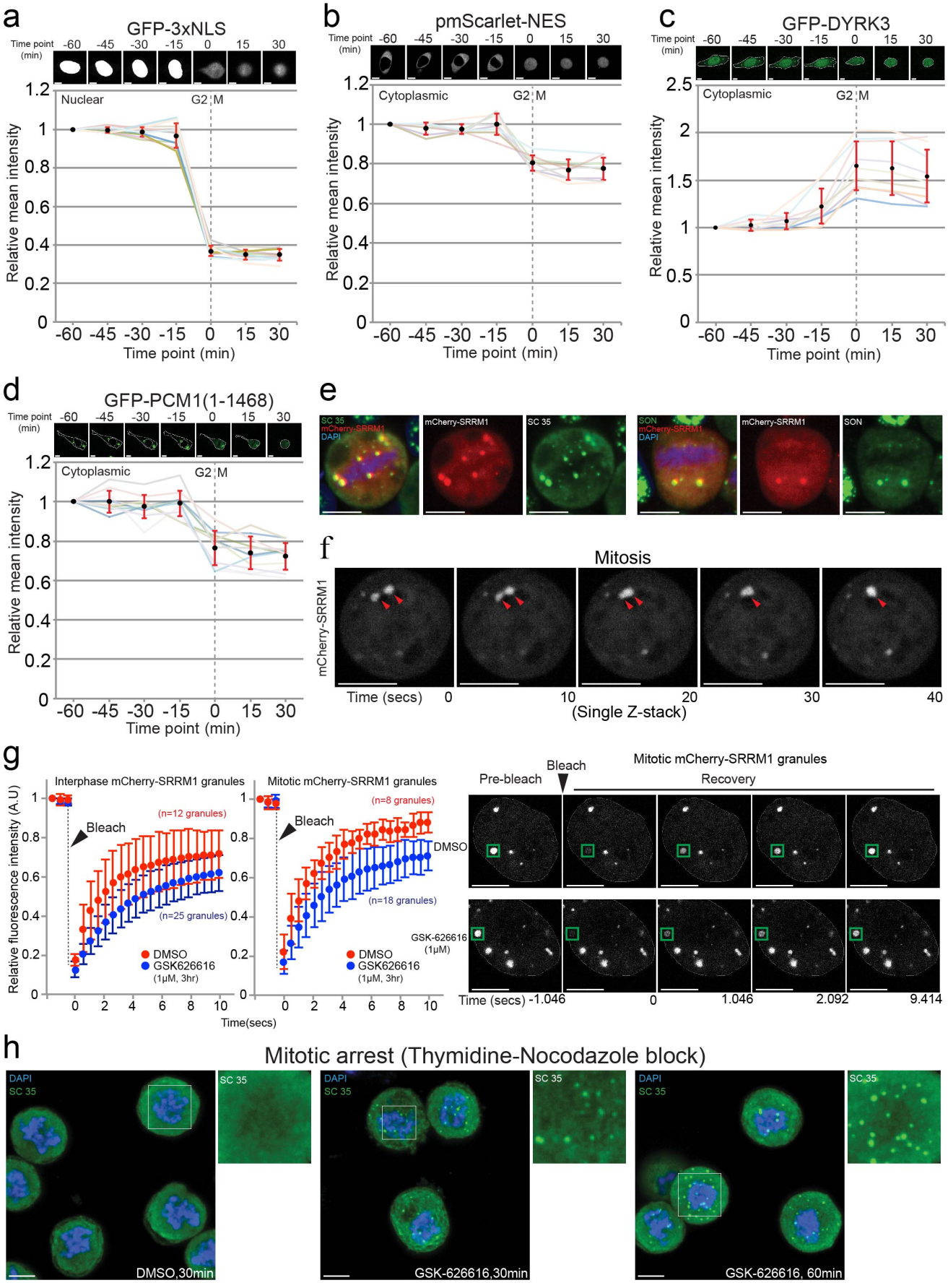

Extended data 9

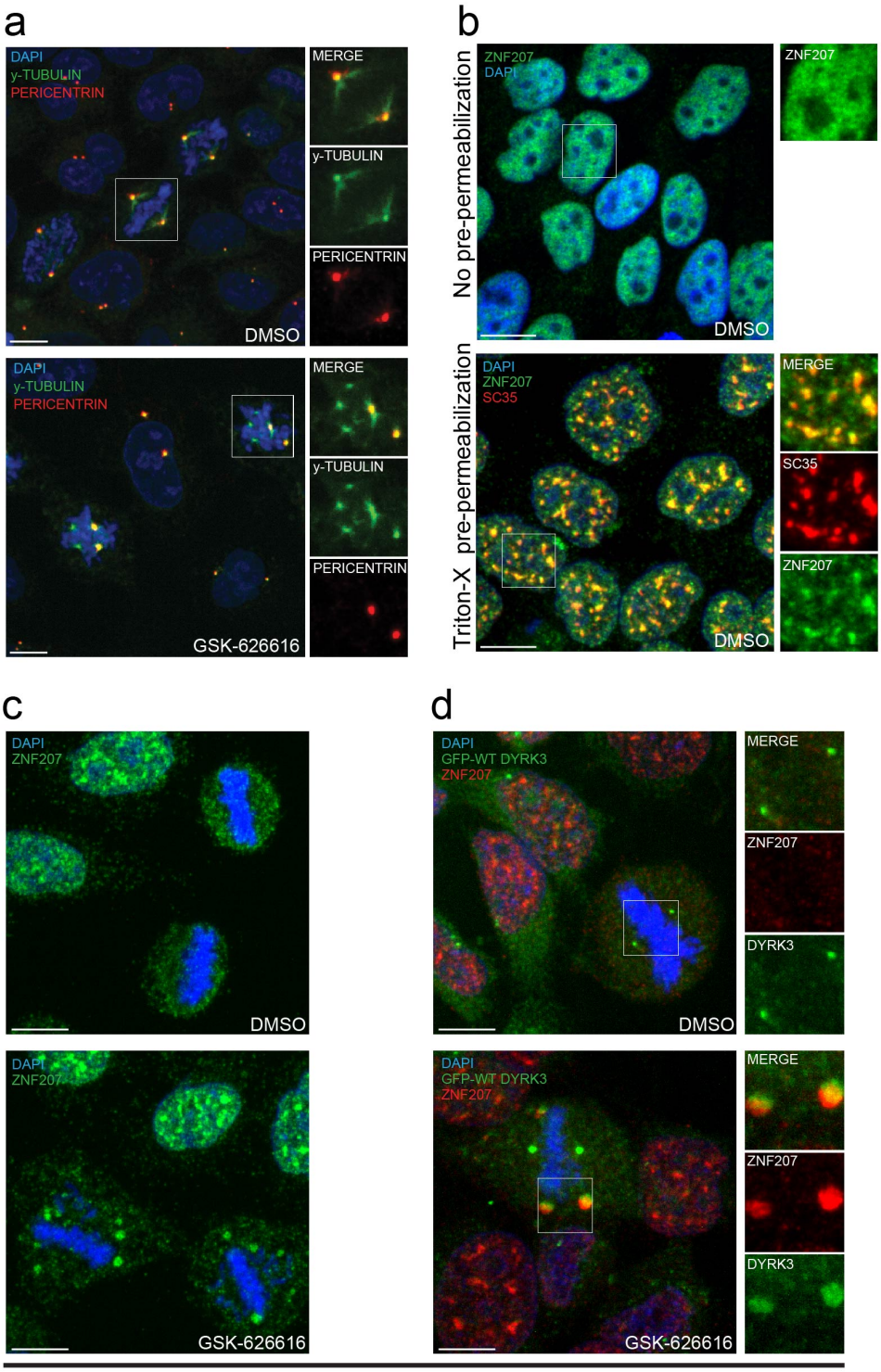

Extended data 10